The Astrophysical Journal, 835:254 (22pp), 2017 February 1 doi:10.3847/1538-4357/835/2/254

The Grism Lens-amplified Survey from Space (Glass). IX. The Dual Origin of Low-mass Cluster Galaxies as Revealed by New Structural Analyses

Takahiro Morishita[1,2,3], Louis E. Abramson[1], Tommaso Treu[1], Benedetta Vulcani[4], Kasper B. Schmidt[5], Alan Dressler[6], Bianca M. Poggianti[7], Matthew A. Malkan[1], Xin Wang[1], Kuang-Han Huang[8], Michele Trenti[4], Maruša Bradač[8], and Austin Hoag[8]
[1] Department of Physics and Astronomy, UCLA, 430 Portola Plaza, Los Angeles, CA 90095-1547, USA; mtaka@astro.ucla.edu
[2] Astronomical Institute, Tohoku University, Aramaki, Aoba, Sendai 980-8578, Japan
[3] Institute for International Advanced Research and Education, Tohoku University, Aramaki, Aoba, Sendai 980-8578, Japan
[4] School of Physics, The University of Melbourne, VIC 3010, Australia
[5] Leibniz-Institut für Astrophysik Potsdam (AIP), An der Sternwarte 16, D-14482 Potsdam, Germany
[6] The Observatories of the Carnegie Institution for Science, 813 Santa Barbara Street, Pasadena, CA 91101, USA
[7] INAF-Astronomical Observatory, I-35122 Padova, Italy
[8] University of California Davis, 1 Shields Avenue, Davis, CA 95616, USA
Received 2016 July 1; revised 2016 December 6; accepted 2016 December 8; published 2017 February 1

Abstract

Using deep *Hubble Frontier Fields* imaging and slitless spectroscopy from the *Grism Survey from Space*, we study 2200 cluster and 1748 field galaxies at $0.2 \leqslant z \leqslant 0.7$ to determine the impact of environment on galaxy size and structure at stellar masses $\log M_*/M_\odot > 7.8$, an unprecedented limit at these redshifts. Based on simple assumptions —$r_e = f(M_*)$—we find no significant differences in half-light radii (r_e) between equal-mass cluster or field systems. More complex analyses—$r_e = f(M_*, U-V, n, z, \Sigma)$—reveal local density ($\Sigma$) to induce only a $7\% \pm 3\%$ (95% confidence) reduction in r_e beyond what can be accounted for by $U-V$ color, Sérsic index (n), and redshift (z) effects. Almost any size difference between galaxies in high- and low-density regions is thus attributable to their different distributions in properties other than environment. Indeed, we find a clear color–r_e correlation in low-mass passive cluster galaxies ($\log M_*/M_\odot < 9.8$) such that bluer systems have larger radii, with the bluest having sizes consistent with equal-mass star-forming galaxies. We take this as evidence that *large-r_e* low-mass passive cluster galaxies are recently acquired systems that have been environmentally quenched without significant structural transformation (e.g., by ram pressure stripping or starvation). Conversely, ∼20% of *small-r_e* low-mass passive cluster galaxies appear to have been in place since $z \gtrsim 3$. Given the consistency of the small-r_e galaxies' stellar surface densities (and even colors) with those of systems more than ten times as massive, our findings suggest that clusters mark places where galaxy evolution is accelerated for an ancient base population spanning most masses, with late-time additions quenched by environment-specific mechanisms mainly restricted to the lowest masses.

Key words: galaxies: clusters: general – galaxies: elliptical and lenticular, cD – galaxies: evolution – galaxies: structure

Supporting material: machine-readable table

1. Introduction

In terms of a host of properties—color, star formation activity, structure, morphology—clusters harbor different galaxy populations than average ("field") environments (e.g., Hubble & Humason 1931; Dressler 1980). The mechanisms that produce these differences have been the subject of intense scrutiny. While evidence of environmental effects has been seen (e.g., Vollmer et al. 2009; Abramson et al. 2011; McPartland et al. 2016; Poggianti et al. 2016), their roles and relative importance compared to in situ galaxy evolution remain poorly understood. Indeed, the extent to which clusters are agents that halt galaxy evolution, as opposed to *tracers* of regions where it has been accelerated, is still under debate (see Peng et al. 2010 with Dressler 1980; Thomas et al. 2005; Guglielmo et al. 2015; Abramson et al. 2016).

One confounding factor is that galaxy-by-galaxy analyses reveal almost no differential environmental effects for systems, e.g., at fixed stellar mass (M_*) and color (Grützbauch et al. 2011). That is, while galaxy *populations* are different in low- and high-density regions, representatives of all parts of parameter space seem to exist everywhere (e.g., Dressler et al. 2013, 2016; Wu et al. 2014).[9] This appears to hold even for scaling laws that (seemingly) should contain the signatures of any transformational mechanism, such as the star formation rate–mass and size–mass relations (e.g., Maltby et al. 2010; Peng et al. 2010; Huertas-Company et al. 2013; Koyama et al. 2013; Allen et al. 2016; but see Vulcani et al. 2010; Paccagnella et al. 2016, who define environment by spectroscopic membership as opposed to spatial overdensity).

However, a key obstacle to many previous investigations has been their relatively high mass limits of $\log M_*/M_\odot \gtrsim 10$. In this regime, a system's self-gravity is strong, perhaps protecting it from environmental influences such as ram pressure stripping or harassment (e.g., Dressler & Gunn 1983; Moore et al. 1996; Treu et al. 2003; Lin et al. 2014). Furthermore, high-mass galaxies might be subject to internal processes—such as feedback from active galactic nuclei, or the suppression of star formation by morphological structures—that act before they enter the cluster, preventing the latter from having any effect at all (e.g., Martig et al. 2009; Hopkins et al. 2014). To better constrain the physical processes *causally related* to environmental density, targeting the low-mass tail of the Galaxy population ($\log M_*/M_\odot \ll 10$) is key.

Some studies of the nearest clusters have probed this regime: Misgeld & Hilker (2011, see also Ferrarese et al. 2006) examined the size–mass relation of Local Group and Coma

[9] Excluding the very most- and very least-massive red objects—dwarf ellipticals and cDs/BCGs—which may never exist in isolation (Koester et al. 2007; Geha et al. 2012).

galaxies at $\log M_*/M_\odot \gtrsim 6$, and Lisker et al. (2009) and Toloba et al. (2015) explored the diversity of dwarf galaxies (dEs, dSphs) in Virgo, with the latter study using kinematical/chemical information to find the evidence of ram pressure stripping-influenced evolution. However, at $z \approx 0$, cluster galaxies are so uniformly old that the residual signatures of any transformational mechanisms may be detectable only in the most detailed fossil evidence (McDermid et al. 2015). Shifting focus to $z \sim 0.5$ would alleviate this issue by probing an epoch when clusters were still rapidly assembling, and hence more dramatically reshaping their galaxy populations (Butcher & Oemler 1978). The recent advent of ultra-deep multi-band imaging and spectroscopy from space enables such studies of low-mass, mid-z galaxies for the first time.

In this paper, we use data from the *Hubble Frontier Fields* (HFF; Lotz et al. 2016) and *Grism Survey from Space* (GLASS; Schmidt et al. 2014a; Treu et al. 2015) to examine the Galaxy populations of clusters and the field at $0.2 \leqslant z \leqslant 0.7$ to a hitherto unexplored mass limit of $\log M_*/M_\odot > 7.8$.

We exploit these data to study the dependence of galaxy size on stellar mass and other structural properties as a function of environmental density using an unprecedented sample of over 3900 cluster and field galaxies. We examine these correlations because: (1) processes that depend on environment—e.g., ram pressure stripping, or mergers (rarer in richer systems)—affect galaxy size and structure in significant and well-defined ways (van Dokkum et al. 2010; Damjanov et al. 2011; Newman et al. 2012; Nipoti et al. 2012; Patel et al. 2013, and many others), and (2) the depth and resolution of new *HST* imaging enables analyses of galaxy structure that current ground-based observations cannot support. This is especially true in the near-infrared, which most directly probes galaxies' stellar mass distributions.

By using a new multidimensional approach that holistically examines galaxies in their natural parameter space—spanning color, size, structure, environmental density, and redshift—our analysis provides a new look at both rapid and long-term environmental influences, yielding a "4D" view of the Galaxy population at unexplored masses and spatial resolutions.

We organize our discussion around the central question posed above: how many of the observed differences in cluster/field populations reflect phenomena *driven* by clusters versus those *traced* by them?

Ultimately, our results suggest that, while a cluster-specific process similar to ram pressure stripping is indeed operational now, ∼20% of present-day passive cluster galaxies with $\log M_*/M_\odot < 10$ must have been "built into" the cluster population at very early times. These findings support a scenario in which clusters mark places where galaxy evolution has been accelerated compared to—but not radically divergent from—the cosmic mean, but are now also in a phase of transforming mainly low-mass systems via environmentally specific phenomena.

We proceed as follows: in Section 2, we describe the observations and measurements upon which our analysis is based. In Section 3, we explore the canonical size–mass relations of our sample and use these to identify important spatiotemporal trends in the data. In Section 4, we adopt a new framework to reinterpret galaxy structural parameters holistically across all environments, performing a multidimensional analysis similar in spirit to the approach that led to the discovery of the fundamental plane (Djorgovski & Davis 1987; Dressler et al. 1987) and the more-fundamental plane (Bolton et al. 2007; Auger et al. 2010) of early-type galaxies. We discuss our results in Section 5 and summarize in Section 6. Details of various parts of our analysis are also provided in Appendices.

Magnitudes are quoted in the AB system (Oke & Gunn 1983; Fukugita et al. 1996). We assume $\Omega_m = 0.3$, $\Omega_\Lambda = 0.7$, $H_0 = 70\ \mathrm{km\ s^{-1}\ Mpc^{-1}}$, and a Chabrier (2003) initial mass function (IMF). The catalog for galaxy structural parameters are made available as an electronic table associated with this paper and through the GLASS website.[10]

2. Data

2.1. Imaging and Spectroscopy

We base our analysis on HFF imaging and GLASS *HST* spectroscopy for the first four HFF clusters with complete data: Abell 2744 ($z = 0.308$), MACS0416 (0.396), MACS0717 (0.548), and MACS1149 (0.544). HFF imaging spans ACS F435/606/814W through WFC3IR F105/125/140/160W filters (seven bands), reaching a 5-σ limiting point-source depth of $m_{\mathrm{F160W}} \approx 28.7$ (Kawamata et al. 2016; Lotz et al. 2016). Both programs use a parallel strategy where WFC3IR and ACS are exposed simultaneously so that the former falls on the cluster core (hereafter "CLS") and the latter on a low-density infall/field region ("PR1"). HFF provided WFC3IR (ACS) follow-ups on PR1 (CLS), so all photometric data are available in both regions.

GLASS spectroscopy consists of 10-orbit G102 + 4-orbit G141 WFC3 grism observations covering the CLS pointings (containing the vast majority of our cluster sample) from which we derive spectroscopic redshifts (z_{spec}). All PR1 redshifts are photometric (z_{phot}; Section 2.3). All GLASS spectra are visually inspected for quality. Here, we make use only of "high quality" redshifts; i.e., those with quality flag $f_{\mathrm{Q}} \geqslant 3$ as described in Schmidt et al. (2014a) and Treu et al. (2015).

It is worth noting that, due to the limited WFC3IR field of view, our observations probe only the *cores* of clusters, i.e., out to $R_{\mathrm{cl}} \sim R_{500} \sim 0.4$ Mpc at $z \sim 0.5$. These are, in some sense, the most extreme galaxy environments in the universe, and the locations where environmental processes (e.g., ram pressure stripping) are most effective. At the same time, PR1 observations sample close to mean-density environments ("the field"), at least at all redshifts distinct from that of the CLS cluster. Hence, our sample exhibits almost maximal density contrast, so our analysis should be quite sensitive to environmental effects.

To increase our field sample size, we also include multi-band *HST* imaging conducted by the *eXtreme Deep Field* (XDF) team (Illingworth et al. 2013). The XDF encompasses one WFC3IR pointing in GOODS-south, which we use to extend our field galaxy sample. These data are of comparable depth to the HFF and include the F775W and F850LP filters in addition to the HFF complement. Ground-based spectroscopic and *3D-HST* grism redshifts (van Dokkum et al. 2013; Momcheva et al. 2016) are incorporated where available.

2.2. Photometry and Catalog Construction

After PSF-matching all images to F160W resolution (FWHM = 0.″18), we stack the data, weighted by rms, to maximize detections of faint (low-mass) galaxies. This composite image is then run through SExtractor (Bertin &

[10] http://glass.astro.ucla.edu

Arnouts 1996) as the detection image. After removing the intracluster light (ICL; see Appendix A), photometry is conducted on the individual images based on the detection locations.

To maximize signal-to-noise ratios (S/N) and thus optimize $z_{\rm phot}$ estimates, fluxes in each filter are determined within fixed apertures of 12 pixels (0.″7) in diameter. When estimating absolute quantities—such as stellar masses—these measurements need to be scaled to account for light outside the aperture. We do this by adopting FLUX_AUTO from SExtractor as the total flux of each galaxy (see Section 2.5). All photometry is corrected for galactic extinction using the Schlegel et al. (1998) dust maps.[11]

Below, we analyze only objects with $m_{\rm F160W} < 26$ mag. Most of this sample has $S/N_{\rm F160W} > 8$, sufficient for accurate stellar mass and structural parameter estimates (Schmidt et al. 2014b, see Appendix D). We have verified that our results are quantitatively robust to this cut-off. The magnitude criterion corresponds to a mass completeness limit of $\log M_*/M_\odot \sim 7.8$ (Section 2.5).

2.3. Spectroscopic and Photometric Redshifts

Wherever available, we adopt public spectroscopic redshift ($z_{\rm spec}$) provided by several authors (Owers et al. 2011; Ebeling et al. 2014; Balestra et al. 2015).[12] We supplement these with GLASS $z_{\rm spec}$. As mentioned, we include only GLASS redshifts with $f_{\rm Q} \geqslant 3$, corresponding to two or more line detections (e.g., [O III] and Hα; Treu et al. 2015). These cover 7% of the $m_{\rm F160W} < 26$ sample (269 galaxies). GLASS redshifts show excellent agreement with the ground-based measurements.

For galaxies lacking $z_{\rm spec}$, we derive photometric redshift ($z_{\rm phot}$) using the seven-band *HST* photometry discussed above. We fit all spectral energy distributions (SEDs) using the EAZY code (v.1.01; Brammer et al. 2008), implemented with emission line/dusty spectrum templates based on the recipe of Ilbert et al. (2009). Given the depth of the HFF data, 85% of our sample has 3-σ detections in more than four bands, supporting reliable $z_{\rm phot}$ estimates.

2.3.1. Photo-z Priors

The only modification we make to the default EAZY fitting routine is to apply different priors for CLS and PR1 objects. In PR1, where field galaxies dominate, we apply the default EAZY F160W prior derived from Theoretical Astrophysical Observatory (TAO) lightcones (Bernyk et al. 2016).[13] In CLS, we modify this prior in order to account for the existence of each cluster as follows.

$$p(z \mid m_{\rm F160W}, z_{\rm cls}) = f \times p(z \mid m_{\rm F160W})_{\rm fld} + (1-f) \times g(z \mid z_{\rm cls}, \sigma), \quad (1)$$

where $p(z \mid m_{\rm F160W})_{\rm fld}$ is the default (field) EAZY prior, f is the fraction of field versus cluster galaxies at a given magnitude (Equation (8)), and $g(z_{\rm cls}, \sigma)$ is a normalized Gaussian centered at the redshift of a given cluster ($z_{\rm cls}$) with a dispersion $\sigma = 2000$ km s^{-1} (about twice the velocity dispersion of each cluster). We set f to the number of galaxies in the PR1 pointing over that in the CLS pointing in bins of $m_{\rm F160W}$, assuming that the CLS sample is dominated by cluster members. Appendix B provides further details.

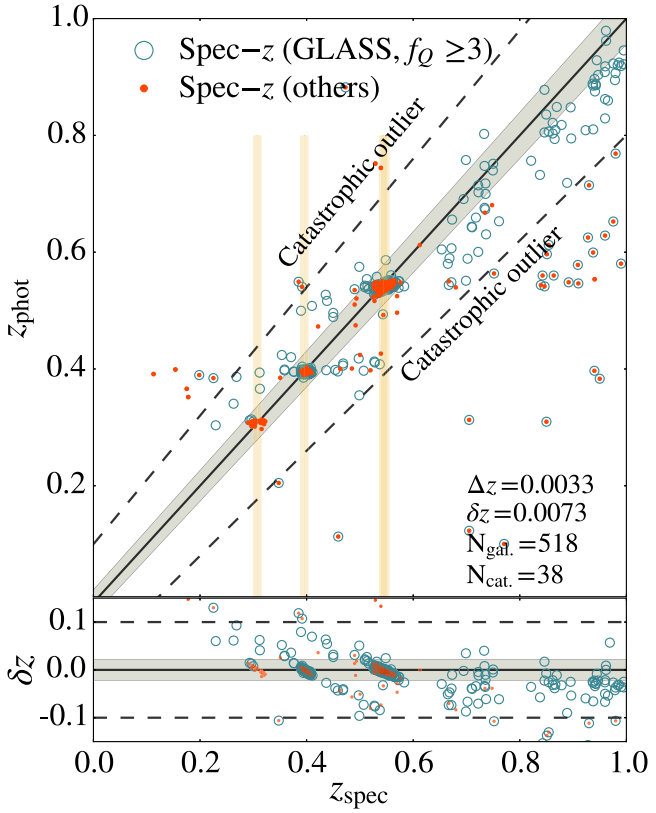

Figure 1. Comparison between photometric ($z_{\rm phot}$) and spectroscopic redshifts ($z_{\rm spec}$) for 518 objects at $z < 1.0$. Spectroscopic redshifts are taken from ground-based measurements if available (red points), and from the GLASS catalog otherwise (blue circles; 242 galaxies with quality flag $f_{\rm Q} \geqslant 3$). Catastrophic outliers have $|z_{\rm spec} - z_{\rm phot}|/(1+z_{\rm spec}) > 0.1$ and lie above or below the dashed lines. These were excluded from the calculation of the median offset, Δz, and the normalized median absolute deviation, δz, of the quantity $(z_{\rm spec} - z_{\rm phot})/(1+z_{\rm spec})$. The gray shaded region corresponds to $3 \times \delta z$. Vertical bands mark the redshifts of the four clusters analyzed with widths corresponding to their velocity dispersions ($\sim$2000 km s^{-1}). Our photometric redshifts are in excellent agreement with $z_{\rm spec}$ for both cluster and field galaxies.

We adopt the z_peak EAZY output as our $z_{\rm phot}$ estimate. We compare the best-fit $z_{\rm phot}$ to $z_{\rm spec}$ in Figure 1, finding a median offset of $\langle (z_{\rm spec} - z_{\rm phot})/(1+z_{\rm spec}) \rangle = 0.003$, and a median absolute deviation $\delta z_{\rm phot} = 0.0073$ (i.e., 0.7%) for galaxies at $z < 1.0$. The cluster $z_{\rm phot}$ prior is partially responsible for this tight dispersion, but $\delta z_{\rm phot}$ rises to just 1.8% in the PR1 and XDF fields where it is not employed, giving us high confidence in the accuracy of our $z_{\rm phot}$ estimates.

Catastrophic outliers are defined to have $|z_{\rm spec} - z_{\rm phot}|/(1+z_{\rm spec}) > 0.1$; they comprise 7.3% of the $z_{\rm spec}$ sample.

After culling to $0.2 \leqslant z \leqslant 0.7$—a redshift range bracketing the four HFF clusters—our final catalog consists of 3948 galaxies, with 2200 in clusters and 1748 in field environments. A total of 298 have ground-based and 168 have GLASS spectroscopic redshifts.

2.4. Cluster and Field Sample Selection

Cluster members are identified using the redshifts described above. As spectroscopic and photometric estimates have different uncertainties, we define different criteria for

[11] https://ned.ipac.caltech.edu/forms/calculator.html
[12] http://www.stsci.edu/hst/campaigns/frontier-fields/FF-Data
[13] https://tao.asvo.org.au/tao/

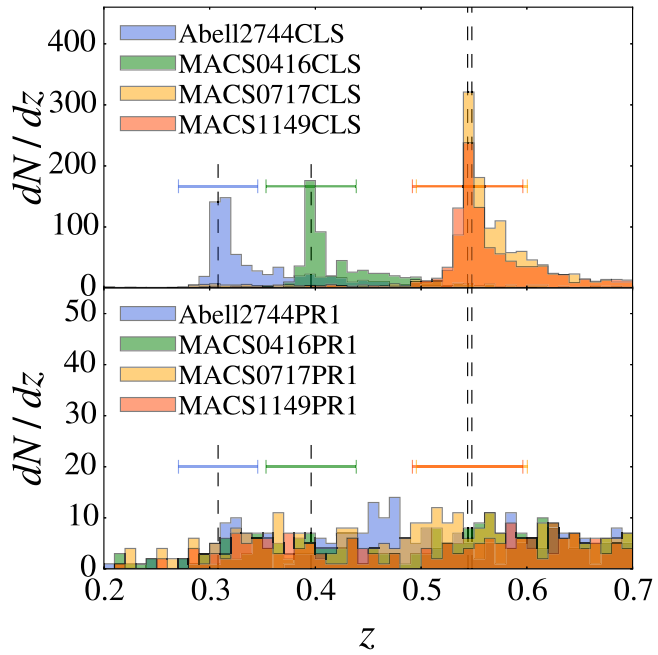

Figure 2. Top: $z_{\rm phot}$ distributions of galaxies in the four cluster-core (CLS) pointings. Histograms are color coded by cluster, with black dashed lines indicating the spectroscopic mean redshift of each ($z_{\rm cls}$). Galaxies within $\pm 3\delta z_{\rm phot.} \times (1 + z_{\rm cls})$ (horizontal bars) are classified as cluster members. Bottom: same as the top panel, but for PR1 sources.

membership based on the metric:

$$\delta z_{\rm incl} \equiv \frac{|z - z_{\rm cls}|}{1 + z_{\rm cls}}. \quad (2)$$

Members have:

1. $\delta z_{\rm incl} \leqslant 0.0084$ or 0.0087 for ground- or space-based $z_{\rm spec}$, respectively, corresponding to double the typical cluster velocity dispersion (i.e., $\sim$2000 km s^{-1}), convolved with measurement errors.
2. $\delta z_{\rm incl} \leqslant 0.0219$ for $z_{\rm phot}$, corresponding to $3 \times \delta z_{\rm phot}$ (see Section 2.3).

We verified that the selected cluster galaxies mostly belong to the red sequence down to $m_{\rm F160W} \sim 25$ mag in the color–magnitude diagram (not shown), giving us confidence in the selection. Figure 2 shows the sample's redshift distribution.

2.5. Stellar Masses

Stellar masses for all galaxies are derived from their multi-band photometry (SED fitting), and $z_{\rm spec}$ or $z_{\rm phot}$ estimate (Section 2.3), using FAST (Kriek et al. 2009). This process requires fluxes to be scaled from aperture measurements ($F_{\rm aper}$; see Section 2.2) to the total values ($F_{\rm tot}$) assuming:

$$F_{\rm tot} = F_{\rm aper} \times \frac{F_{\rm auto}^{\rm F160W}}{F_{\rm aper}^{\rm F160W}}, \quad (3)$$

where $F_{\rm auto}^{\rm F160W}$ is the total flux (FLUX_AUTO) from SExtractor, covering 3 Kron radii (Kron 1980).

This procedure works for 92% of the sample, but for the rest the FLUX_AUTO uncertainties are large enough (mainly due to close, bright neighbors or ICL residuals) that using it risks introducing a bias. In these cases—S/N($F_{\rm auto}^{\rm F160W}$) $\leqslant$ 1—we apply no scaling. This affects stellar mass estimates very little as the original 0.″7 aperture encompasses $\sim 2\, r_e$ for most of these systems.

We use the stellar population models of Bruzual & Charlot (2003), assuming solar metallicity, a Chabrier (2003) IMF, and a Calzetti et al. (2000) dust law. Internal extinction is calculated assuming $0 \leqslant A_V \leqslant 4$ mag with a grid spacing of 0.1 mag. We adopt exponentially declining star formation histories —SFR(t) $\propto \exp(-t/\tau)$—with $\log \tau$ yr$^{-1} \in [8, 10]$ in steps of 0.2 dex. Uncertainties are taken as the 1-σ limits derived by FAST.

2.6. Rest-frame Colors

We wish to examine how environment affects both galaxy structure and star formation. An efficient means of classifying galaxies by their star formation state is by their location in rest-frame $U - V/V - J$ ("*UVJ*") color–color space (Williams et al. 2009). These colors are directly calculated by convolving the best fit EAZY spectral templates with Johnson U, V, and 2MASS J-band filters. We follow Williams et al. (2009) and define red (quiescent) galaxies to have:

$$\begin{aligned} U - V &> 0.88 \times (V - J) + 0.69, \\ U - V &> 1.3, \\ V - J &< 1.6. \end{aligned} \quad (4)$$

We refer to all others as blue (star-forming) galaxies.

Figure 3 shows the distribution of our sample—split by mass ($\log M_*/M_\odot \lessgtr 9$) and environment—in *UVJ* space. We see not only the bimodality of passive/star-forming galaxies, but also the trend of increasing passive fraction with stellar mass, as expected. We note also that, at low stellar mass, cluster passive galaxies appear slightly redder than their field counterparts. We return to this point in Section 5.2.

2.7. Cross-checking Photo-z Accuracy: Galaxy Number Counts and Passive/Star-forming Fractions

Figure 4, top, shows the stellar mass distributions of our samples. Our purpose here is not to investigate, e.g., the best-fit Schechter parameters, but rather to demonstrate the robustness of our largely $z_{\rm phot}$ based cluster/field sample separation.

Comparing our field results (right) with those from Muzzin et al. (2013) in a similar redshift range ($0.2 < z < 0.5$), we see good consistency at $\log M_*/M_\odot \geqslant 8.3$, the completeness limit of the previous study. This is true for all galaxies, and both passive and star-forming sub-classes, suggesting that our field sample is indeed representative of the general galaxy population and not excessively contaminated by cluster objects.

Figure 4, bottom-left, shows the fraction of passive galaxies for cluster and field environments as a function of stellar mass. There is a significant excess in clusters over the entire mass range, rising from $\sim$50% at $\log M_*/M_\odot \approx 8$ to over 90% at $\log M_*/M_\odot > 10$. This is also as expected from previous spectroscopic studies (e.g., Dressler et al. 2013, their Figure 16), and suggests that our cluster sample is not excessively diluted by field galaxies.

Interestingly, the bottom-right panel in Figure 4 shows that, even within our sample's rather narrow redshift range ($0.3 \lesssim z_{\rm cls} \lesssim 0.6$), evolution in the cluster passive fraction—the Butcher & Oemler (1978) Effect—is detected. The evolution is observed only for low-mass systems ($\log M_*/M_\odot < 9.0$), which might suggest that environmental effects are most pronounced for these systems. We combine

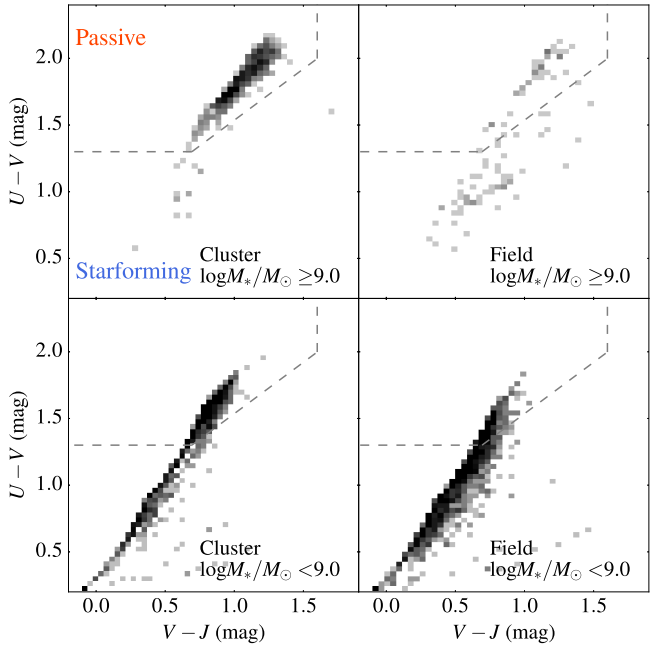

Figure 3. Rest-frame *UVJ* diagrams for cluster (left) and field (right) galaxies, with masses $\log M_*/M_\odot \geq 9$ (top) and <9 (bottom). Galaxies in the top-left box (dashed lines; from Williams et al. 2009) in each panel are classified as passive; the remaining galaxies we define as star-forming. A clear trend of increasing passive fraction with both stellar mass and environmental density emerges as expected, but we also find low-mass passive cluster galaxies to be redder than those in the field.

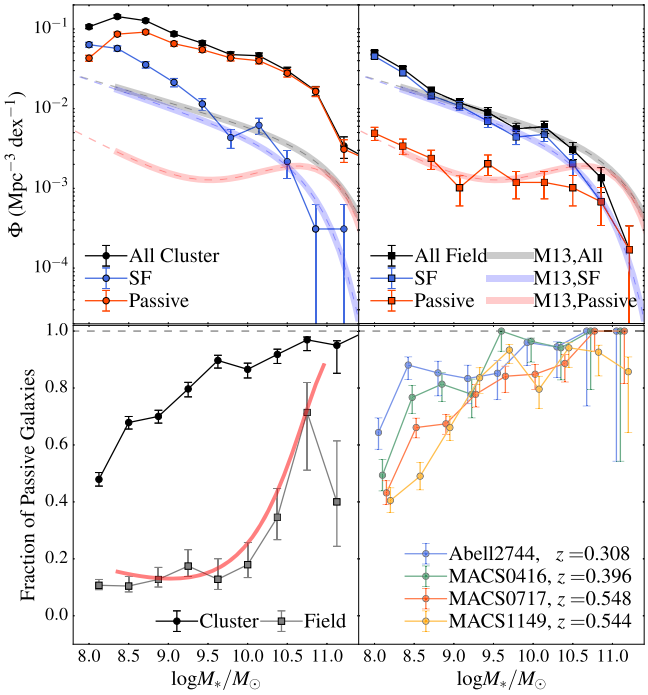

Figure 4. Top: stellar mass functions of cluster members (left) and field galaxies (right), color-coded by population (black = all, blue = star-forming (SF), red = passive). Error bars assume a binomial distribution. Results from Muzzin et al. (2013) for field galaxies at $0.2 < z < 0.5$ are shown for comparison (colored consistently). Bottom left: fraction of passive galaxies as a function of stellar mass for cluster members (black) and field galaxies (gray). The Muzzin et al. (2013) field result is shown as the red solid line. Our measurement diverges from those authors' at the highest stellar mass, but our sample of such objects is very small. Bottom right: fraction of passive galaxies for each of our four clusters. The population of low-mass galaxies ($\log M_*/M_\odot < 9$) evolves even in the narrow redshift range these span (or ~2 Gyr of cosmic time).

this result with our inferred galaxy structural properties to develop a preferred scenario for the origin and evolution of these low-mass passive cluster systems in Section 5, but regardless: all of the above results suggest that our field/cluster galaxy sample selection process is accurate.

2.8. Structural Parameters

Galaxy structural parameters—half-light radii (r_e), axis ratios ($q \equiv$ semiminor/semimajor axis), and Sérsic indices (n)—are estimated by fitting single Sérsic profiles (Sérsic 1963) using GALFIT (Peng et al. 2002). Initial guesses for the relevant parameters derive from the SExtractor output.

Although we discuss only the F160W structural parameters here—corresponding to rest-frame wavelengths of ~1.0 μm at $z \sim 0.5$—we perform fits in all *HST* bands to consistently estimate the ICL properties (Appendix A). After subtracting the ICL from the original CLS image, we then re-estimate the structural parameters for those galaxies and adopt the second-round values. In PR1, we adopt the initial fitting results.

During fitting, we constrain centroids and magnitudes to within 3 pixels (in x and y) and 1 mag of the SExtractor input values. We also set $1 < r_e/\text{pixel} < 150$ ($0.4 < r_e/\text{kpc} < 60$ at $z \sim 0.5$), $0.1 < n < 8$ (Sérsic index), and $q > 0.2$. "Successful" fits are those whose derived parameters fall within these limits. Failures are excluded from further analysis. Close-neighbors—objects with centroids within 6″ of target galaxies—are fit simultaneously.

We also visually inspect outliers which reside 2-σ above/below the size–mass relations of each population (see next section), and exclude 132 galaxies whose fits are substantially affected by proximity to very bright galaxies/belong to a blended pair, or have grossly distorted morphologies. Our final catalog contains 2636 galaxies with robust structural parameters. This corresponds to a mean success rate of ~68%, rising from ~64% at $\log M_*/M_\odot \sim 8.0$ to >80% at $\log M_*/M_\odot \sim 10.0$. Appendix D provides further details of the fitting procedure. Structural properties, with SED fitting parameters, are shown in Table 1 and available online.

3. Canonical Size–mass Relation Analysis

While we will ultimately adopt a more sophisticated description (Section 4), we begin our analysis of environment's influence on galaxy size and structure by examining "canonical" size–mass relations: i.e., by splitting the sample into four populations—passive/star-forming, cluster/field—and comparing linear fits to their $\log r_e$–$\log M_*$ correlations. We model the samples with a simple regression

$$\log\left(\frac{r_e}{\text{kpc}}\right) = \alpha + \beta \log\left(\frac{M_*}{10^9\, M_\odot}\right) + N(\sigma), \quad (5)$$

where α and β are the relation's intercept (at $10^9\, M_\odot$) and slope, and $N(\sigma)$ is a Gaussian describing its intrinsic dispersion assuming that sizes are lognormally distributed at fixed stellar mass (e.g., Newman et al. 2014).

We use standard Bayesian techniques to derive the posterior probability of the parameters—including the intrinsic scatter—using a Monte Carlo Markov Chain (MCMC) solver (see Appendix E).

Table 1
GLASS Size–mass Relations: Source and Structural Catalog

ID_{cls}	ID_{id}	α_{J2000}	δ_{J2000}	z_{best}	F160W mag	$\log M_*/M_\odot$	$\log r_e/$ kpc	$\log n$	$\log b/a$	f_{GALFIT}	$(U-V)$ mag	Σ_{5th} Mpc^{-2}						
1	1225	3.5751052	−30.3789048	0.32	25.322	0.079	7.56	0.095	0.01	0.1262	0.9031	0.4286	−0.3188	0.1537	0	1.384	0.701	79.994
1	1227	3.5750756	−30.377077	0.31	18.429	0.0004	10.44	0.01	0.6893	0.05	0.5623	0.05	−0.4815	0.05	0	2.002	1.26	414.472
1	1228	3.57345	−30.3779341	0.31	19.837	0.0012	9.85	0.01	0.3876	0.0014	0.6609	0.0038	−0.2676	0.05	0	1.889	1.186	613.999
1	1231	3.5751362	−30.3785238	0.31	21.42	0.0038	9.12	0.025	0.6115	0.0076	0.6096	0.0171	−0.1024	0.0055	0	1.719	1.011	969.508
1	1537	3.5719139	−30.377392	0.31	21.362	0.0044	9.13	0.01	0.2536	99.0	0.1239	99.0	−0.2441	99.0	0	1.696	0.968	381.979
1	1694	3.5775421	−30.3788716	0.31	21.148	0.0031	9.31	0.01	0.1411	0.0002	0.1931	0.0028	−0.1871	0.05	0	1.825	1.064	652.593
1	1711	3.6095439	−30.3821106	0.29	17.929	0.0003	10.57	0.01	0.2158	0.0003	0.433	0.0016	−0.1367	0.05	0	2.069	1.417	10.539
1	1720	3.5898065	−30.3784113	0.33	24.616	0.0721	7.9	0.015	0.2149	0.0035	0.316	0.0147	−0.1487	0.0061	0	1.474	0.742	36.944
1	1756	3.5891816	−30.3789491	0.31	22.77	0.0122	8.58	0.04	0.1786	0.0006	0.233	0.0025	−0.0862	0.05	0	1.486	0.79	129.734
1	1763	3.5976371	−30.3792022	0.31	20.411	0.0027	9.6	0.01	0.323	0.0001	0.49	0.0014	−0.3768	0.05	0	1.824	1.14	110.436
1	1797	3.5788573	−30.3794304	0.31	23.845	0.023	8.15	0.035	0.0052	0.0018	0.0414	0.0118	−0.0088	0.0044	0	1.532	0.772	374.076
1	1804	3.579726	−30.3795369	0.31	23.316	0.0166	8.38	0.07	0.2024	0.0008	0.0792	0.0036	−0.2596	0.05	0	1.517	0.848	238.311
1	1823	3.571678	−30.3797062	0.31	23.53	0.0131	8.3	0.02	−0.2747	0.0012	0.2504	0.0098	−0.0506	0.0049	0	1.676	0.881	613.999
1	1830	3.5953954	−30.3804029	0.31	19.449	0.0008	9.92	0.01	0.5365	0.0003	0.4871	0.0014	−0.2676	0.05	0	1.719	1.056	271.209
1	1853	3.5792236	−30.380187	0.3	23.613	0.0224	8.21	0.01	0.2104	0.0011	−0.0132	0.0089	−0.1427	0.006	0	1.574	0.784	44.584

Note. (a) Cluster ID. 1: Abell2744CLS 2: MACS0416CLS 3: MACS0717CLS 4: MACS1149CLS 5: Abell2744PR1 6: MACS0416PR1 7: MACS0717PR1 8: MACS1149PR1 99: XDF. (b) ID for individual objects. (c) z_{best} is ground-based spectroscopic redshift if available, implemented with GLASS grism redshift, and photometric-redshift derived by EAZY for else. (d) F160W-band Auto magnitude derived by SExtractor. (e) Stellar mass derived by FAST. (f) F160W-band structural parameters derived by GALFIT. (g) Visual inspection flag for sources 2σ above/below the size-mass relation for each population. 0: Fine 1: Contaminated 2:Point sources. (h) Rest-frame $U-V$, $V-J$ colors derived by convolving best-fit templates by EAZY. (i) Fifth-closest local galaxy number density. Only a portion of this table is shown here to demonstrate its form and content.

(This table is available in its entirety in machine-readable form.)

We fit the samples over the entire mass range, but note that σ and all parameter uncertainties decrease when the sample is split at $\log M_*/M_\odot \sim 9.8$ (see Section 3.3), and the low- and high-mass objects fit separately (Table 2). This suggests that these populations may be fundamentally different. Sections 3.4 and 5 explore this statement further.

3.1. Size–mass Relations of Four Populations

Figure 5 shows the derived linear size–mass relations (Equation (5)) for the four populations: passive and star-forming galaxies in clusters and the field. Outliers excluded from the analysis are plotted as open boxes (see Section 2.8, Appendix A). The best-fit slopes are derived with each point weighted by its measurement error (see Appendix E). Figure 6 and Table 2 summarize the results.

For either star-forming or passive galaxies, we find identical slopes and intercepts in both cluster-core and field environments within the uncertainties, suggesting—as previously seen (e.g., Huertas-Company et al. 2013; Vulcani et al. 2014)—that environment *seemingly* does not affect galaxy size (at fixed mass, population, and time) down to $\log M_*/M_\odot \sim 8$. Furthermore, while we recover the expected correlations of stellar mass and Sérsic index (e.g., from Lang et al. 2014) for both sets of galaxies (color-coding in Figure 5; see also Section 3.2), there is no obvious difference in Sérsic index trends in clusters or the field, suggesting that environment *also* does not affect galaxy structure.

Notably, our derived slopes for passive systems are much shallower than those found previously in either the local universe ($\beta \sim 0.6$ by Shen et al. 2003) or at similar redshifts to our sample's ($\beta \sim 0.7$ by van der Wel et al. 2014, fit over $\log M_*/M_\odot \gtrsim 10$). As detailed in Section 3.3, this finding is driven by our low mass-completeness limit—$\log M_*/M_\odot = 7.8$—hitherto unexplored at $z \sim 0.5$.

3.2. Structural Parameters on the Size–mass Diagram

Besides size, galaxies' structures can encode the action of evolutionary mechanisms. We now explore this aspect of our systems as parameterized by the Sérsic index, n.

Figure 7 shows the median and 16th–84th percentile spreads in n for passive/star-forming cluster/field galaxies as a function of stellar mass. As was true for their sizes (Section 3.1), star-forming cluster and field galaxies display almost identical trends, implying that entrance into or life inside the cluster (at late times) induces little if any structural transformation in these systems.

We also see that the Sérsic index distributions for low mass ($\log M_*/M_\odot < 9.5$) passive and star-forming galaxies overlap significantly in both environments, though passive galaxies—especially in clusters—are offset systematically to slightly higher n values. Such structural similarities of low-mass star-forming and passive galaxies supports a scenario where low-mass passive systems do not arise through violent mechanisms—such as mergers—but instead gentle phenomena. Alternatively (or additionally), they are most consistent with having been drawn exclusively from the high-n tail of the star-forming galaxy population, modulo the effects of disk fading. We return to these points in Section 5.

3.3. Two Populations of Passive Cluster Galaxies

The results above show that galaxies in the highest density regions of the universe do not differ systematically in the size–mass–Sérsic index plane from those in mean density environments. However, this does not mean that clusters do not influence galaxy growth, nor does it mean that they do not trace special regions of the universe. The comparisons so far have been gross examinations of four samples at the same epoch. Yet, the mechanisms that either are transforming or have transformed the cluster population with respect to that of the field (Figure 4) may act too subtly—or have acted too long ago—to probe in the above fashion. Can we find any evidence for this in our data?

To do so, we take two steps. First, we turn our attention exclusively to the low-mass tail of the cluster population: as mentioned in Section 1, these systems should be most affected by environment-specific mechanisms (harassment, strangulation, stripping). Second, in the next section, we study the sizable ($\simeq$0.25 dex) *scatter* of the size–mass relation: it is clearly significant, so perhaps it encodes important information.

Splitting the sample at $\log M_*/M_\odot \sim 9.8$,[14] where the slope seems to change, we fit the less- and more-massive galaxies separately with the formula in Equation (5). Figure 8 shows the results for passive cluster galaxies.

Here, we see that low-mass passive cluster galaxies exhibit a much milder, nearly flat slope of $\beta_1 = 0.11 \pm 0.01$. Put differently, galaxies in this regime increase in size by a factor of 1.7 for every factor of 100 in stellar mass. This is much shallower than either the slope for massive passive galaxies—$\beta_2 \sim 0.51$ (consistent with previous studies; e.g., Shen et al. 2003)—or star-forming galaxies of any mass in any environment ($\beta \sim 0.2$; e.g., van der Wel et al. 2014; Allen et al. 2016; Annunziatella et al. 2016). Notably, the inferred intrinsic scatter decreases from $\sigma = 0.27 \pm 0.01$ of the single slope fitting to $\sigma_1 = 0.20 \pm 0.01$ for low-mass, and $\sigma_2 = 0.23 \pm 0.01$ for high-mass galaxies when these systems are fit separately. All best-fit results are listed in Table 2.

These findings qualitatively support previous studies that find the low-mass passive population to have a shallower size–mass relation slope in the local universe (e.g., Binggeli et al. 1984; Ferrarese et al. 2006; Omand et al. 2014) and at $z \sim 0.5$ (e.g., van der Wel et al. 2014). Ferrarese et al. (2006) is especially relevant as it is a much more highly resolved *HST* study of Virgo cluster galaxies. These authors identify a similarly flat trend—$d\log(r_e)/dM_B = -0.05 \pm 0.02 \Rightarrow \beta \approx 0.125$ for galaxies with $M_B \lesssim -20$ ($\log M_*/M_\odot \lesssim 10.5$, assuming M/L_B from Bell et al. 2003, at $B - R = 1.4$. See their Equation (21) and Figure 117, top-right). Later studies of Virgo dwarf galaxies by Lisker et al. (2009) and Toloba et al. (2015) confirm these findings. Ultimately, we will concur with van der Wel et al. (2014) and Toloba et al. (2015) in suggesting that some of these objects are likely environmentally stripped low-mass late-types (but also Lisker et al. 2009 in that some *are not*; Section 5), but, irrespective of any mechanism, a break in this relation suggests the existence of two classes of passive galaxies with distinct formation paths: one with a steep size–mass slope indicative of nearly constant stellar surface density ($\beta = 0.5$; Hubble 1926) and therefore perhaps a single formation time, and one with a shallow slope ($\beta_1 \approx 0.1$) indicative of a broad range of (*mostly*

[14] Shifting the border $\pm$0.1 dex does not affect the result.

Table 2
GLASS Size–mass Relations: Best-fit Coefficients

Region	Type	α Single Slope	β	σ	α_1 Double Slope	β_1 (Low-mass)	σ_1	α_2 Double Slope	β_2 (High-mass)	σ_2
Cluster	Passive	$0.150^{+0.009}_{-0.008}$	$0.169^{+0.008}_{-0.012}$	$0.270^{+0.006}_{-0.006}$	$0.109^{+0.006}_{-0.006}$	$0.111^{+0.009}_{-0.014}$	$0.197^{+0.005}_{-0.007}$	$-0.302^{+0.045}_{-0.043}$	$0.513^{+0.032}_{-0.028}$	$0.231^{+0.014}_{-0.010}$
Cluster	Star-forming	$0.360^{+0.014}_{-0.018}$	$0.189^{+0.019}_{-0.019}$	$0.275^{+0.011}_{-0.013}$	$0.333^{+0.018}_{-0.018}$	$0.179^{+0.018}_{-0.017}$	$0.228^{+0.008}_{-0.008}$	$0.092^{+0.120}_{-0.162}$	$0.395^{+0.136}_{-0.093}$	$0.187^{+0.020}_{-0.041}$
Field	Passive	$0.168^{+0.011}_{-0.014}$	$0.150^{+0.016}_{-0.016}$	$0.224^{+0.009}_{-0.013}$	$0.133^{+0.021}_{-0.020}$	$0.078^{+0.018}_{-0.024}$	$0.184^{+0.009}_{-0.010}$	$-0.067^{+0.134}_{-0.133}$	$0.340^{+0.091}_{-0.091}$	$0.213^{+0.016}_{-0.031}$
Field	Star-forming	$0.373^{+0.010}_{-0.013}$	$0.223^{+0.012}_{-0.014}$	$0.251^{+0.004}_{-0.006}$	$0.350^{+0.011}_{-0.013}$	$0.210^{+0.014}_{-0.015}$	$0.216^{+0.004}_{-0.007}$	$0.343^{+0.082}_{-0.073}$	$0.225^{+0.063}_{-0.066}$	$0.197^{+0.019}_{-0.020}$

Note. Summary of the best-fit coefficients for single slope ($\log r_e/\mathrm{kpc} = \alpha + \beta \log(M_*/10^9\,M_\odot) + N(\sigma)$; see Equation (5) in the main text) and double-slope fit (same as Equation (5), but subscript 1 for $\log M_*/M_\odot < 9.8$ and subscript 2 for $\log M_*/M_\odot \geqslant 9.8$ galaxies).

Table 3
GLASS Size–mass Relations: Best-fit Coefficients for the Holistic Fitting (Equation (7) and Figure 11)

α	β_{M_*}	β_n	$\beta_{\rm UV}$	β_{Σ_5}	β_z	σ
$0.122^{+0.005}_{-0.005}$	$0.254^{+0.007}_{-0.008}$	$-0.041^{+0.019}_{-0.020}$	$-0.286^{+0.014}_{-0.014}$	$-0.031^{+0.006}_{-0.007}$	$-1.059^{+0.142}_{-0.130}$	$0.205^{+0.003}_{-0.003}$

lower) stellar surface densities, and therefore a range of formation times.

We note that the similarly shallow slope is also observed for the passive *field* galaxies (Table 2), where environmental processes are thought to be subtle. In this case, the shallow slope for low-mass galaxies would not be attributed to the environmental effect. However, low-mass passive field galaxies in this study could be in similar environments with cluster member galaxies, because we have grouped the sample into the two subgroups by using the same FoV. Actually, Geha et al. (2012) found that most low-mass passive galaxies are in group (or denser) environments by using the local sample, and so would be affected by processes similar to those affecting the low-mass cluster sample. Our *genuine* field sample, which resides in PR1 and XDF regions, is statistically weak and larger data sets will be required to fully address this question.

3.4. Toward a Formation Pathway: Star-forming Galaxies as a Model for Passive Galaxies

In any scenario, passive galaxies were star-forming at some epoch. Hence, we can use the star-forming galaxy size–mass relation derived above as a model for the sizes that passive galaxies *should* have if they had stayed in the star-forming population. Residuals from this exercise—the difference between how big the passive galaxies are and how big they are predicted to be—may contain important information about how, when, and therefore why they diverged from their star-forming peers.

Figure 8 compares the size–mass relation of passive cluster galaxies with the mean relation for star-forming galaxies at several redshifts taken from van der Wel et al. (2014). Points are color-coded by the rest-frame $U - V$ color. This quantity is a good indicator of the time since a galaxy's last episode of star formation (at least out to $\sim$4 Gyr for low-mass objects, assuming the local stellar mass–metallicity relation of Kirby et al. 2013 holds at $z \sim 0.5$) and therefore serves as a clock counting back to when any red galaxy was last in the star-forming population. Evidently, only the largest of the passive low-mass systems have sizes compatible with equal mass star-forming (field) galaxies near the epoch of observation ($0.2 \leqslant z \leqslant 0.7$), and are therefore consistent with being drawn from that population. The sizes of some very high mass passive systems are also comparable with those of star-forming galaxies at the same epoch, but since the former are giant ellipticals, effectively all of their other properties rule them out from having descended from the latter.

Figure 9 explores these findings in greater detail, showing the size *difference* of passive cluster galaxies from the star-forming relation at $z \sim 0.5$ (taken from van der Wel et al. 2014). Boxes highlight the median $U - V$ colors in 0.2×0.1 dex boxes. The horizontal lines also shown are the predicted offsets derived from the size-mass relations at different redshifts also from van der Wel et al. (2014).

A concern here is that, as seen in the left panel of Figure 5, star-forming galaxies exhibit a color–mass trend, such that more massive star-forming objects are redder. Hence, the observed color gradients in Figure 9 might reflect a baseline mass–color covariance in the star-forming (source) population, not a true third parameter.

To correct for this, we fit the mass–color relation for star-forming galaxies, obtaining:

$$U - V/\mathrm{mag} = 1.03 + 0.11 \log\left(\frac{M_*}{10^9\, M_\odot}\right). \quad (6)$$

As shown in the right panel of Figure 9, even after applying this correction to the passive cluster galaxies, the color gradient along the y-axis remains, confirming our earlier statement that, to some degree, the spread of passive cluster galaxy sizes at fixed mass reflects a record of *the time* when a system left the star-forming population. As this extends to at least $z \sim 3$ (i.e., $\sim$7 Gyr before the epoch of observation), this gradient can encode quite long timescales (Speagle et al. 2014; Abramson et al. 2016).

A clear, quantitatively robust color gradient is apparent at fixed stellar mass, shown in Figure 10. As clarified by the colored squares in Figure 9, smaller-size passive galaxies are also *redder* than larger-size passive galaxies. This finding amplifies results from Figure 8: at low masses, the largest-size passive galaxies have both sizes *and* colors consistent with their having been been drawn from the star-forming population more recently than their smaller-size passive counterparts.

Taken together, Figures 8–10 present strong evidence that smaller passive galaxies "quenched" earlier, while the largest passive galaxies are quenching now. The same trend is observed in local clusters (e.g., Valentinuzzi et al. 2010, for $\log M_*/M_\odot > 9.8$ galaxies) and in the field (e.g., Poggianti et al. 2013, $\log M_*/M_\odot > 10.3$), with luminosity-weighted age, rather than $U - V$ color, which support our interpretation.

Interestingly, our analysis shows no such gradient for massive passive galaxies ($\log M_*/M_\odot > 9.8$; Figure 10), supporting the idea that they have a different formation history than many low-mass objects, at least in the sense of having been in place long before the epoch of observation. This conclusion is also supported by the nearly uniform stellar surface densities of these objects (Figure 8; $\beta_2 \sim 0.5$ corresponds to $M_*/r_e^2 = $ const.), compared to the large spread of densities in the low-mass population. This homogeneity of massive passive galaxies is also found by Zanella et al. (2016) with *HST* spectroscopic measurements at $z \sim 2$.

These facts—combined with the detailed properties of the massive galaxies' stellar populations (Thomas et al. 2005; McDermid et al. 2015)—suggest an *accelerated* growth channel for the high mass population, rather than environmental quenching, which may dominate at low masses. The low-mass population is converged to a high-mass one at low $\Delta \log r_e$. This may indicate that these low-mass galaxies trace the same channel as the high-mass galaxies. We return to this statement in Section 5.

Our ability to identify and compare this trend with non-cluster low-mass passive galaxies is hampered by the very small sample size. The same exercise reveals a trend in the same direction as in the cluster sample, but with large uncertainties. The mean color of the field systems is bluer than their cluster counterparts at these low masses, another point we will return to in Section 5.

4. A Holistic Analysis of All Galaxies in Higher-dimensional Parameter Space

So far, we have performed a canonical examination of the size–mass relation (Section 3). When separating samples by color and environment a priori, it seems that the relation is not so sensitive to where a galaxy is, but rather *when* it left the star-forming population (Figure 9).

Technically, however, the above comparisons are not the fairest tests of environmental effects. These require matching cluster and field samples in all relevant characteristics—e.g., color, mass, and Sérsic index—leaving environment as the *only* distinguishing trait. Here, we adopt a multidimensional analysis that takes the above factors into account, and thus provides a fair, quantitative assessment of environmental effects.

Combining all galaxies into a single sample, we change our description from one in which mass is the only independent variable to one where a range of other parameters might also influence galaxy size, including: Sérsic index, $U-V$ color, redshift, *and* local number density (i.e., environment). Rather than imposing somewhat artificial boundaries, this procedure allows for a data-driven exploration of the correlations between continuous parameters. The new multidimensional correlation becomes

$$\log\left(\frac{r_e}{\mathrm{kpc}}\right) = \mathscr{M} + N(\sigma), \tag{7}$$

where

$$\begin{aligned}\mathscr{M} \equiv \alpha &+ \beta_{M_*}\log\left(\frac{M_*}{10^9\,M_\odot}\right)\\ &+ \beta_n\log\left(\frac{n}{1.50}\right)\\ &+ \beta_{\Sigma_5}\log\left(\frac{\Sigma_5}{214.0\ \mathrm{Mpc}^{-2}}\right)\\ &+ \beta_z\log\left(\frac{1+z}{1.54}\right)\\ &+ \beta_{\mathrm{UV}}[(U-V) - 1.43\ \mathrm{mag}].\end{aligned}$$

Here, $\Sigma_5 = (5+1)/\pi r_5^2$ is the projected number density (per sq. Mpc) defined over the distance to the 5th closest object, and all variables are fit with respect to the pivot values (medians) in their respective denominators. Figure 11 shows the best-fit relation, whose parameters are listed in Table 3.

The derived coefficients reveal how much galaxy sizes depend on one parameter when the others are held fixed; they effectively describe how samples differ in one property when matched in all others.

From these results, we see that stellar mass and color have the strongest correlations with galaxy size: when $\log M_*/M_\odot$ increases by 1.0 dex, $\log r_e/\mathrm{kpc}$ changes by $\beta_{M_*}\times 1.0 \sim 0.25$ dex; nearly a factor of 2. Similarly, a 1.0 mag increase in $(U-V)$ color results in ∼0.29 dex *decrease* in size, consistent with the results in Figure 9.[15]

In this context, the nearly complete independence of galaxy sizes on environmental density deduced from Figure 6 is made dramatically and quantitatively clear. The best-fit coefficient is $\beta_{\Sigma_5} = -0.031$, corresponding to only $\Delta\log r_e/\mathrm{kpc} < 0.1$ dex (<26%) over the factor of ∼1000 spread in projected density probed by our data ($1 \lesssim 1000$). We stress again that our sample spans normal environments to the densest regions in the universe—cluster cores. Hence, it seems unlikely that a stronger signal could be found by looking elsewhere.

We have confirmed that the residuals produced by applying the globally fit holistic model to the field and cluster subsamples separately are flat, and have a dispersion consistent with that shown in Figure 11. Hence, cluster galaxies with low Σ_5 (e.g., those at large R_{cl}) and non-cluster galaxies with high Σ_5 (e.g., those in groups), do not appear to deviate significantly from expectations derived without knowledge of the global environment.

While these results are consistent with our previous findings based on a simpler analysis, the treatment described here presents several advantages. First, it allows the *data* to identify which correlations are most important, rather than humans using bins based on what we think *should* be relevant. Second, by making all variables explicit, we avoid being misdirected by correlations imposed by hidden parameters.

Indeed, had such an analysis been favored a priori, it would have been immediately evident that any analysis of the effect of environment *at fixed epoch* would provide only partial answers. As shown in Figure 9, most of the well known "environmental" trends are in fact a reflection of differences in galaxy *ages*, and perhaps ancient discrepancies in the mass functions that differentiate the structures that collapsed first in the universe (clusters) and those that do so much later (the field; see Figure 4, also Kelson et al. 2016). Beyond this, the gross appearance of such scaling relations is apparently highly insensitive to any cluster-specific mechanisms.

Combined with the residual color-dependence—a "clock" measuring the time since a passive galaxy left its star-forming peers—this finding reinforces suggestions from the previous analyses that local number density *traces* transformative phenomena to an important extent. That is, it marks regions wherein an initial large-scale overdensity caused all systems within it to evolve rapidly, independent of any late-time *transformative* effects. We discuss this further below.

5. Discussion

So far, we have studied galaxy size and structure in different environments by (1) splitting the sample into four sub-populations (the "canonical" approach; Section 3), and (2) treating them as a single population (the "holistic" approach; Section 4).

Via the first approach, we see no environmental effect on the size–mass relation, even at the unexplored stellar mass limit of $\log M_*/M_\odot = 7.8$ at $z \sim 0.5$. Via the second method, this finding is qualitatively confirmed, and quantitatively contextualized: assuming only that galaxies can be described by a

[15] The largest *absolute* coefficient corresponds to redshift effects —$\beta_z = -1.06$ dex/dex—but, the small z range observed ensures this does not translate to a large impact on measured sizes: a 0.3 dex (2×) change in r_e via redshift evolution alone requires comparing $z \sim 2$ systems to our sample (consistent with Figure 9).

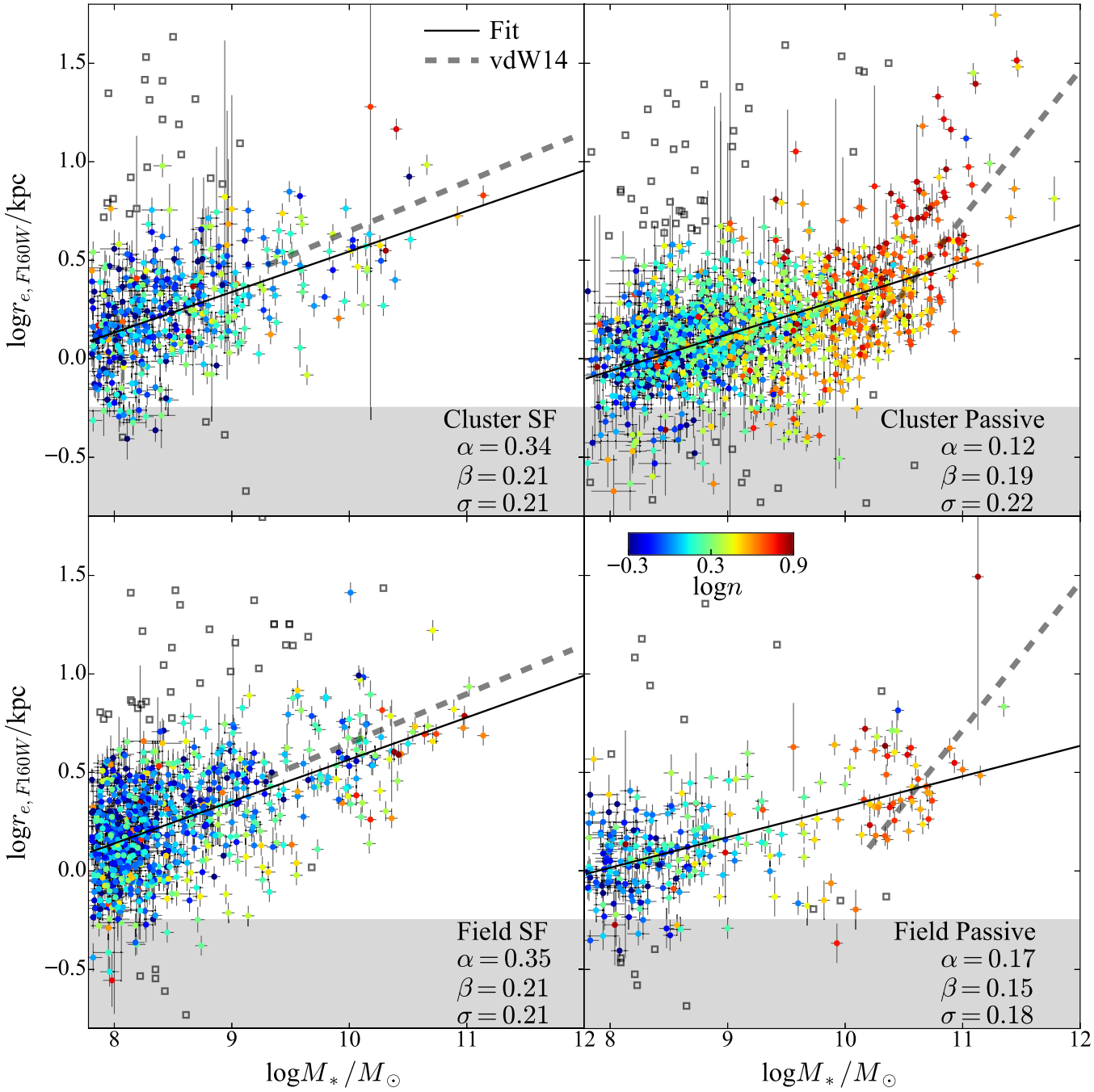

Figure 5. F160W size–mass relation of SF and passive galaxies (left/right, respectively) in clusters and the field (top/bottom). Colors reflect galaxy F160W Sérsic indices ($\log n$). Open squares denote systems with close, large/bright neighbors, which comprise 132 visually inspected outliers, and are excluded from further analysis (Section 2.8). As Figure 8 shows, low- and high-mass passive galaxies have markedly different size–mass relations, hence, due to our inclusion of galaxies with masses as low as $\log M_*/M_\odot = 7.8$, the slopes we obtain for passive galaxies are ∼0.3 dex per dex shallower than previous estimates (e.g., van der Wel et al. 2014, overplotted as black dashes over their fitting range). Size estimates are robust above gray zones at the bottom of all plots, showing $r_e \leqslant \mathrm{FWHM_{F160W}}/2$ at $z = 0.5$ (Morishita et al. 2014).

suite of parameters that should be sensitive to the same phenomena impacting galaxy sizes, we find that environment has perhaps the *smallest* effect.

Figures 8–11 suggest that, for many systems, by the time a galaxy is sufficiently "transformed"—by whatever process—to be identified as "passive," evidence of any direct impact of cluster-specific phenomena is wiped out, or of secondary importance at best.

This seems certainly true for high-mass cluster galaxies ($\log M_*/M_\odot \gtrsim 9.8$), which dominate the cluster's stellar mass content and have stellar populations that are completely incompatible with having been drawn recently from the star-forming population. For low-mass cluster galaxies, however, the picture is more nuanced.

As discussed in Section 3.4 (Figures 9 and 10), the largest-r_e passive cluster galaxies with $\log M_*/M_\odot < 9.8$ have sizes and

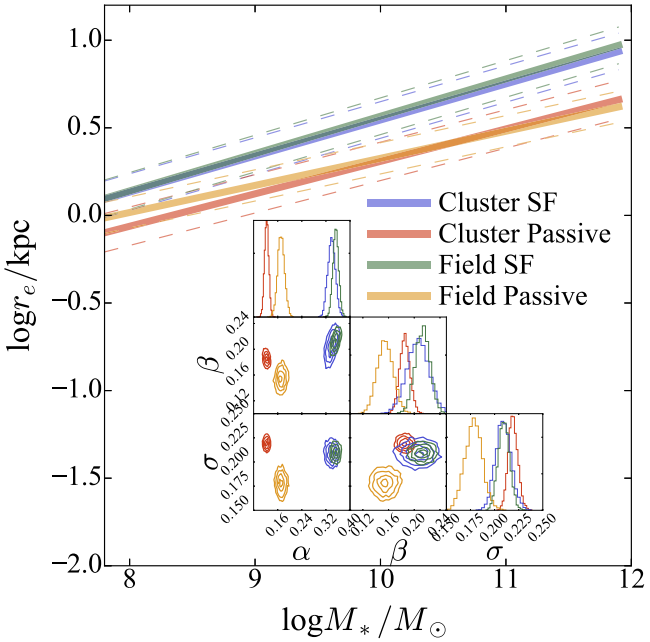

Figure 6. Comparison of the best-fit size–mass relations (Equation (5)) for the four populations considered in Figure 3: cluster passive and star-forming galaxies (red/blue lines); field passive and star-forming galaxies (orange/green lines). Dashed lines show the inferred intrinsic dispersion of the relations, σ. Comparison of the best-fit parameters is shown in the inset. Contours reflect 68%, 96%, and 99% confidence intervals as determined using an MCMC solver.

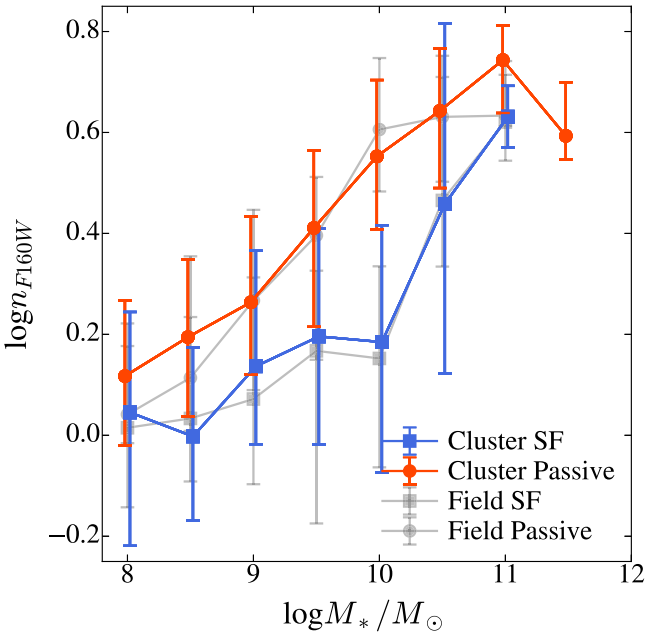

Figure 7. Median and 16th–84th percentile spreads of F160W Sérsic index, n, for cluster star-forming/passive galaxies in bins of stellar mass. Background gray plots are those for field star-forming/passive galaxies. Values for cluster galaxies are replotted in light gray in the right panel for comparison. Star-forming galaxies have similar n distributions at $\log M_*/M_\odot \lesssim 10$, while passive galaxies display a monotonically rising trend.

colors consistent with their having come from the field star-forming population at times close to the epoch of observation. The smallest-r_e galaxies in this population, however, seem to have been in place for many Gyr, perhaps as long as their higher-mass neighbors, suggesting a dual formation scenario for low-mass passive galaxies (see also, e.g., Poggianti et al. 2006).

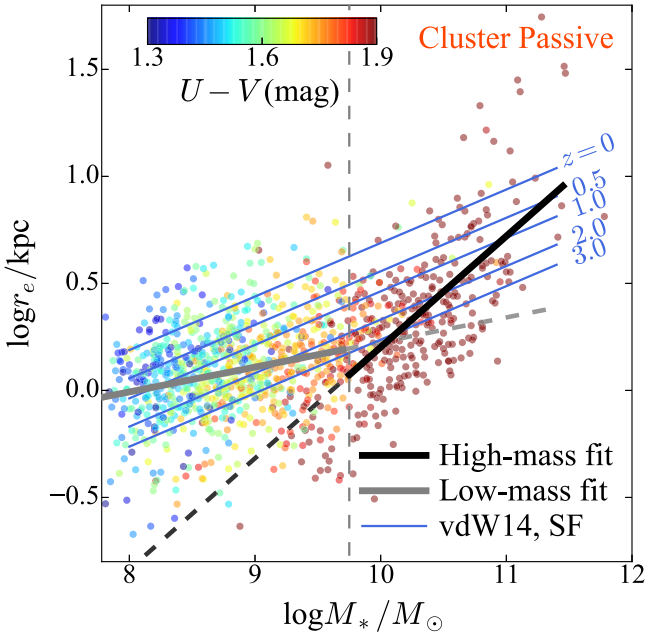

Figure 8. Size–mass relation for red cluster galaxies. Points are color-coded by rest-frame $U-V$ color. We separately fit low- and high-mass systems—split at $\log M_*/M_\odot = 9.8$ (vertical dashed line), where Sérsic index of star-forming galaxies deviate (Figure 7). The low-mass slope (gray line) is almost flat ($\beta_1 = 0.11$), while the high-mass fit (black line) is much steeper ($\beta_2 = 0.51$). Size–mass slopes of *star-forming galaxies* by van der Wel et al. (2014) are overlaid to discuss the star-forming population as a parent sample of passive galaxies.

5.1. Large-r_e Low-mass Passive Cluster Galaxies

On the face of it, the fact that the largest-size low-mass passive galaxies lie near the size–mass relation of star-forming galaxies at the same epoch points immediately to something like ram pressure stripping or starvation (e.g., Wetzel et al. 2013) as the most likely transformative mechanisms. These are indeed cluster-*driven*, relying exclusively on the properties of the mature cluster environment. Four additional facts support this conclusion.

1. Our target clusters are *currently* bright X-ray sources, confirming the presence of dense intra-cluster gas (Mantz et al. 2010). Especially in the core regions probed by the *HST* observations, drag from this hot atmosphere can effectively strip gas from infalling galaxies, and also stifle their accretion of new gas for future star formation, the definitions of ram-pressure stripping and starvation.
2. Large-size, low-mass systems are most amenable to (ram pressure) stripping as their internal gas supplies are most loosely bound (Treu et al. 2003). They would also run out of fuel for star formation relatively quickly if starved of external fuel supplies given the generally higher specific star formation rates of their low-mass star-forming galaxy progenitors (e.g., Salim et al. 2007; Whitaker et al. 2014).
3. The low-mass end of the passive cluster mass function grows over the epochs probed (Figures 4, bottom-right), consistent with a scenario where star-forming galaxies are continually being transformed. This is also consistent with previous studies that a single epoch is disfavored for the formation of low-mass passive cluster galaxies (e.g., Roediger et al. 2011; Toloba et al. 2014).

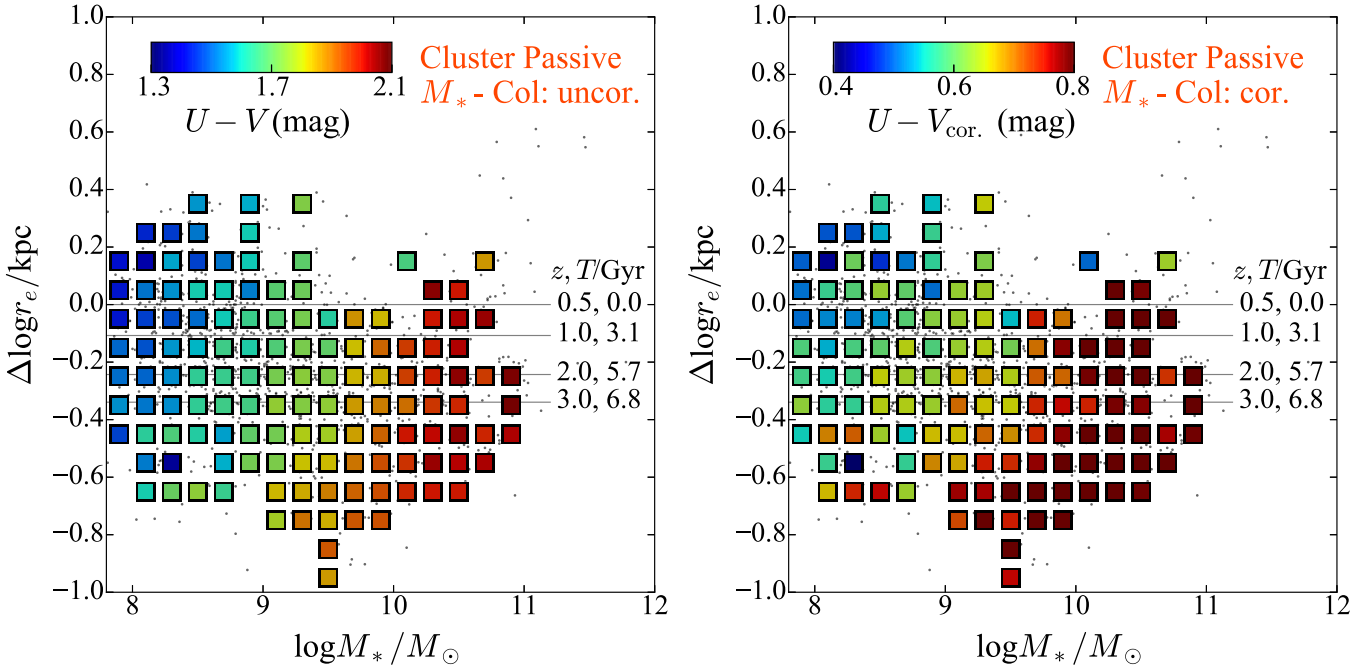

Figure 9. Left: size differences, $\Delta \log r_e$, of passive cluster galaxies from the fit for SF galaxies (points). The horizontal lines are sizes of SF galaxies at different redshifts (printed with T Gyr from the epoch of observation, $z \sim 0.45$; same as blue lines in Figure 8) from van der Wel et al. (2014). Median values for each subspace are shown by the filled squares, color-coded by $U-V$ color, which serves as an age indicator. These show redder colors to correspond with larger offsets from the mean size of SF galaxies at $z \sim 0.5$, suggesting both that (1) smaller-size galaxies are older, and (2) only the largest-size low-mass passive galaxies are consistent with having recently been drawn from the SF population. Right: same as the left but $U-V$ color is corrected for the intrinsic color–mass relation of SF (putative progenitor) galaxies with Equation (6). The color trends along the offset persist after the correction.

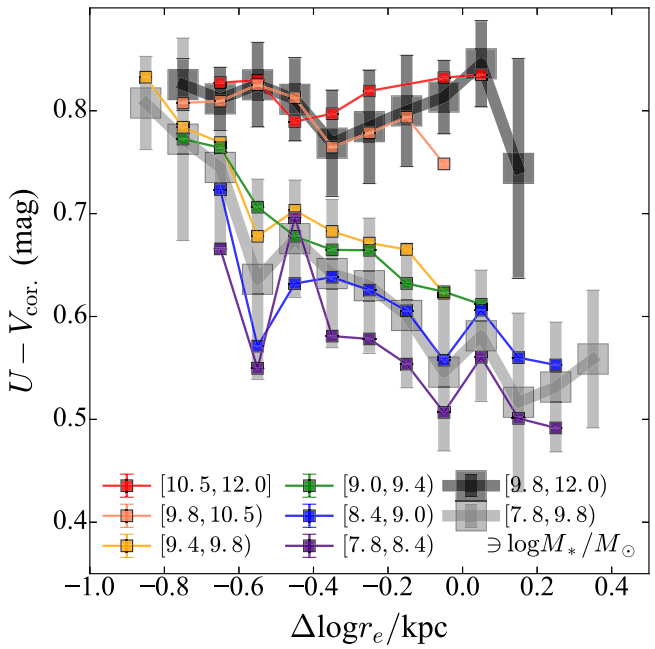

Figure 10. Color trend ($U-V_{\rm cor.}$) along $\Delta \log r_e$ within given stellar mass bins (colored squares), observed in Figure 9. The medians for high-mass ($\log M_*/M_\odot \geqslant 9.8$) and low-mass ($\log M_*/M_\odot < 9.8$) galaxies are shown with larger symbols (black and gray, respectively). The error bars are median absolute deviations. We see a bimodal trend at larger $\Delta \log r_e$ values, where low-mass galaxies are recently quenched from star-forming population, while at smaller $\Delta \log r_e$ values the bimodality is converged.

4. The relatively low Sérsic indices of the low-mass passive cluster galaxies (Figure 7) point to a "gentle" mechanism; one that does not destroy disks/rearrange galaxies' stellar components, which is consistent with starvation, ram pressure stripping, and galaxy harassment (Bialas et al. 2015). The observed Sérsic indices of low-mass passive galaxies are slightly higher than those of star-forming ones with similar stellar mass, but this difference is explained by disk fading, where cessation of star formation in the disk leads to more concentrated light profiles (and thus higher Sérsic indices; Lackner & Gunn 2013).

Given the direct evidence for stripping in local analogues (e.g., Cayatte et al. 1990; Abramson et al. 2011) and at intermediate redshift (Vulcani et al. 2015), it seems likely that at least this mechanism is *currently* operative.

However, to attribute the presence of the smallest-size low-mass passive galaxies—which are *also* the oldest (Figure 9)—to the same mechanism(s), one must take into account the evolution of the cluster itself.

5.2. Small-r_e Low-mass Passive Cluster Galaxies

At $z \sim 3$, when many of these $\log M_*/M_\odot < 9.8$ systems seem last to have been in the star-forming population, our target clusters would have been much less massive, and were therefore home to much more tenuous, cooler intra-cluster media. Based on calculations by Trenti et al. (2008),[16] we estimate that our clusters—systems with $\log M_{\rm halo}/M_\odot \sim 15$ at $z \sim 0.5$—had progenitors with $\log M_{\rm halo}/M_\odot \sim 14$ at $z \sim 3$ (also consistent with Evrard et al. 2002). Hence, the question becomes whether or not the environments at those epochs—when the global density and neutral gas fraction was higher—

[16] ΛCDM cosmology based on *Wilkinson Microwave Anisotropy Probe* (*WMAP*) year 1 results (Spergel et al. 2003).

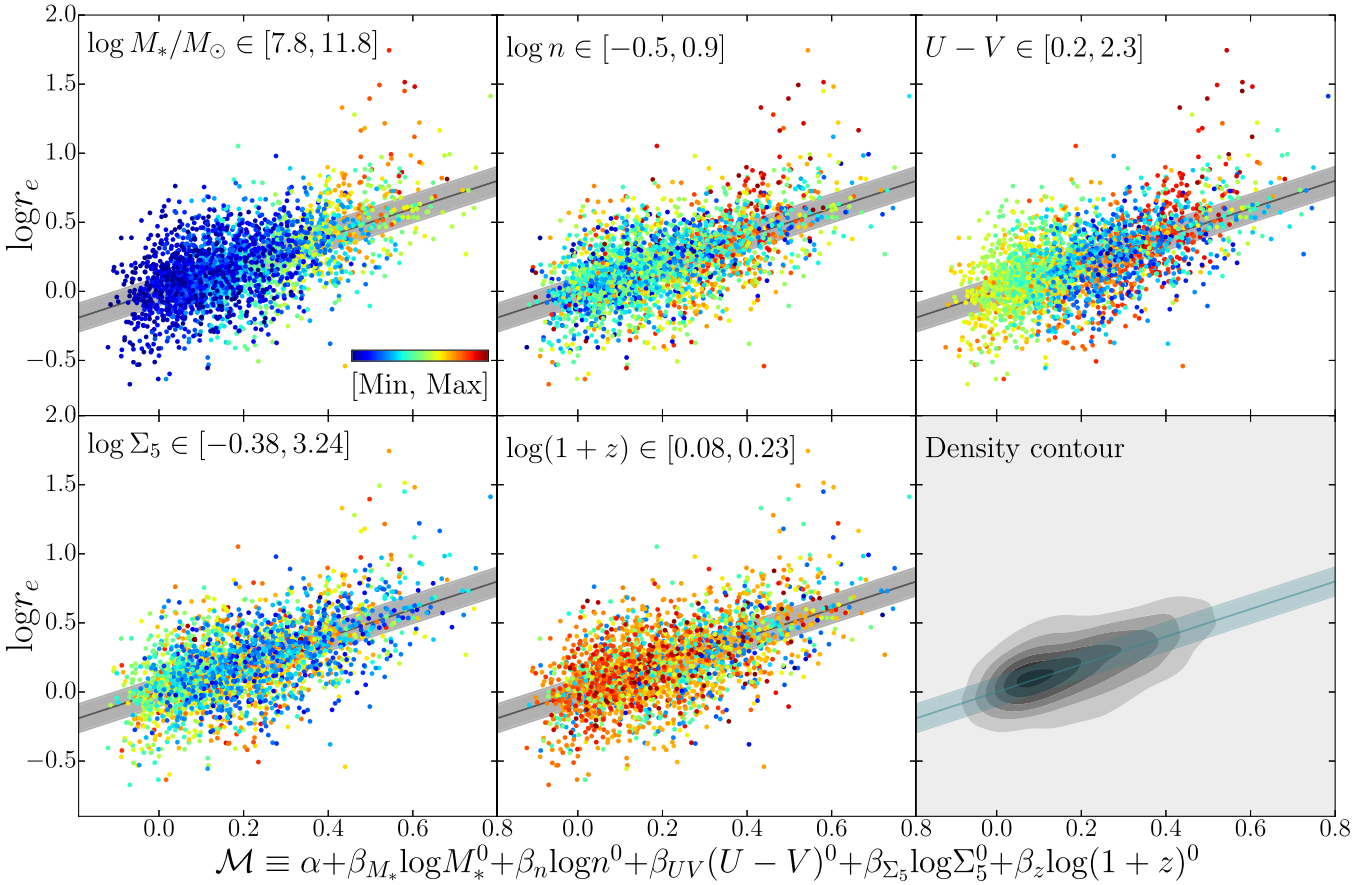

Figure 11. Galaxy size fitted with stellar mass, Sérsic index, $U - V$ color, local density (Σ_5), and redshift (see Equation (7)). In this fitting, galaxies are not split into any sub-categories (e.g., cluster/field, red/blue). ^{0} superscripts in the equation denote that the variables have been normalized to the pivot values (medians) given below Equation (7). We show the same best fit result in 6 panels, but each of which has different color-coded scheme: stellar mass (top left), log n (top middle), $(U - V)$ (top right), log Σ_5 (bottom left), and $\log(1 + z)$ (bottom middle). The contour of galaxy number density is shown in bottom right. The color is coded according to the observed parameter range shown in each bracket ([Min, Max]).

could have supported ram pressure stripping/significantly cut galaxies off from their fuel supplies. If they could, these channels could provide a unified explanation for all low-mass passive cluster galaxies. If they could *not*, another channel must have been open.

To further constrain the strength of the above channels and their ability to produce the smallest low-mass passive cluster galaxies, we can assume all of the evolution of the passive fraction shown in Figure 4, bottom-right, is due to the same mechanism(s) and project the effects back in time. We do so by extrapolating a simple linear regression and show the results in Figure 13. This is an extreme model—we might expect the recent evolution in passive fractions to be more rapid than its past evolution due to the cluster and cosmic evolutionary effects mentioned above, which should reduce the efficiency of, e.g., stripping, with lookback time. However, it provides something like an upper limit to the quenching that could be driven by such mechanisms, which is what we seek.

From this exercise, we obtain $dF_{\rm red}/dt \sim 0.1\,{\rm Gyr}^{-1}$ at $\log M_*/M_\odot < 9$. By extrapolating the slope, we find that the passive fraction at these masses would be zero at $2 \lesssim z \lesssim 4$, depending on the bin. Hence, it could be that *all* cluster (core) galaxies with $\log M_*/M_\odot < 9$ were transformed due to gas removal, or whatever other process is active *now* in clusters.

However, this idea does not hold for even slightly more massive passive cluster galaxies; i.e., those with $9.25 \lesssim \log M_*/M_\odot \lesssim 10.25$—there are simply too many of these to have all arisen through the same channel. Our toy calculation suggests that perhaps 30% of these systems were already in place at $z \sim 3$, just 2 Gyr after the Big Bang. For these galaxies —and presumably those with yet lower masses, assuming a more-realistic nonlinear $dF_{\rm red}/dt$—other explanations must be sought. We explore one possibility below.

5.2.1. Evidence for Accelerated Evolution for Low-mass Dense Cluster Galaxies

Clues for a formation scenario come from the low-mass passive *field* and the high-mass cluster populations.

From Figure 3, we see that, at $\log M_*/M_\odot < 9$, there exist passive galaxies in clusters that are systematically redder than those in the field. This implies that the cluster galaxies reached their final mass before their field counterparts.

Turning to the $\log M_*/M_\odot > 9.8$ passive cluster population, Figure 8 shows the size–mass relation of these objects to lie remarkably close to a line of constant stellar surface density, $\Sigma_* = M_*/r_e^2$. This points to common formation time for these systems (Franx et al. 2008; van den Bosch et al. 2008; Stringer et al. 2014; Abramson & Morishita 2016; Lilly & Carollo 2016;

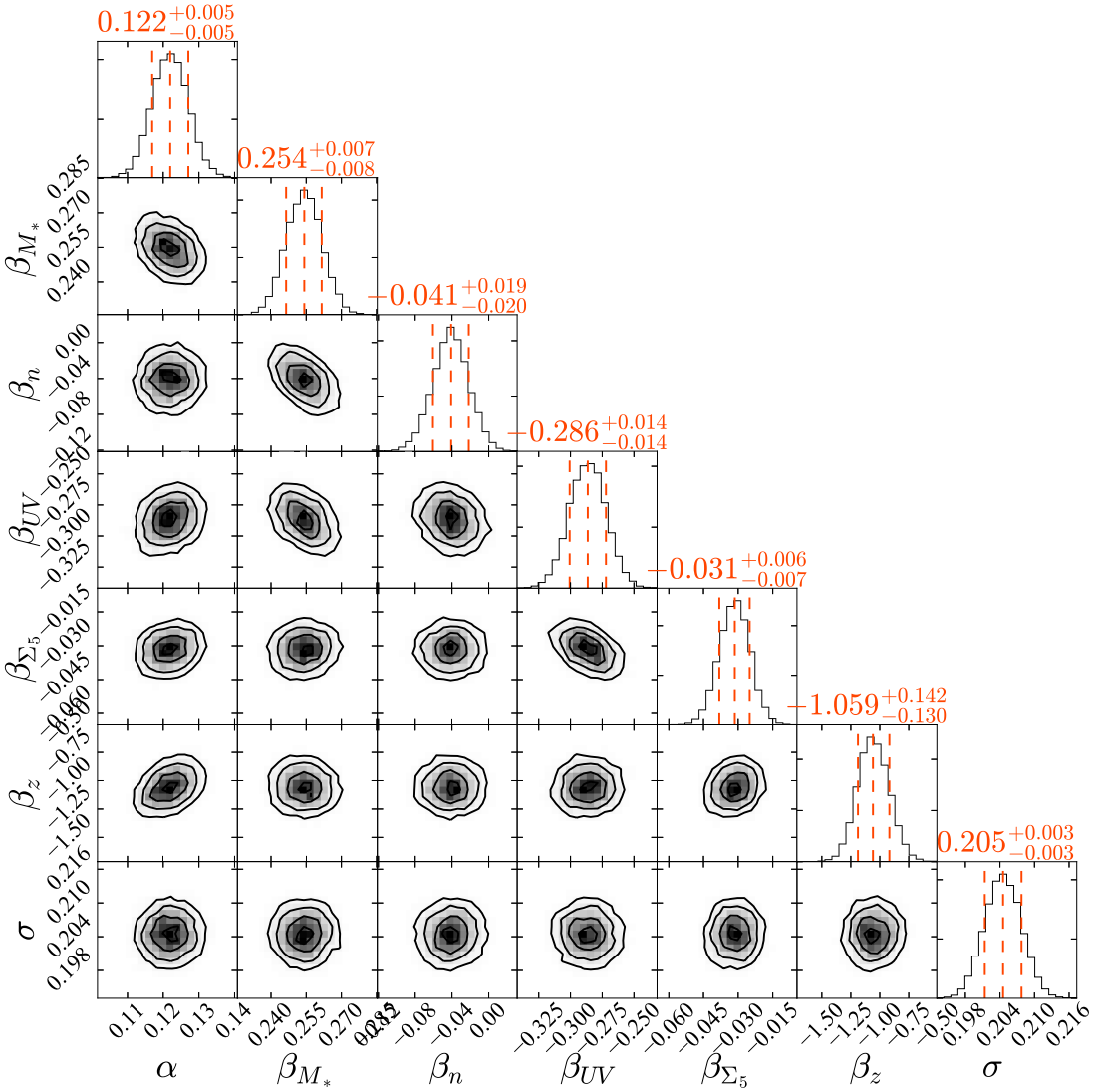

Figure 12. Parameter estimates for the "holistic size–mass relation" (Equation (7)) fit to the full galaxy sample. Contours reflect 68%, 96%, and 99% confidence intervals as determined using an MCMC solver. The best fit coefficient values, 50th percentile, are shown on top of each column with offsets from 16th/84th percentiles. We see no significant degeneracies between the derived coefficients.

Whitaker et al. 2016). Given their uniformly ancient stellar populations (based on their colors), the implication is that such high-mass passive cluster galaxies are monolithically old and do not descend from field galaxies transformed over long stretches of time.

Assuming this is the case, we can obtain a rough idea of how many low-mass objects formed similarly by calculating the fraction of them that have surface densities similar to the high-mass systems. Given that the 2-$\sigma \approx 0.5$ dex intrinsic spread in sizes at fixed mass corresponds to a factor of 100 difference in surface densities for galaxies at the top and bottom of the size–mass relation, we should expect some $\log M_*/M_\odot = 8$–9 passive objects to have densities comparable to their $\log M_*/M_\odot = 10$–11 counterparts.

Indeed, we find ≈18% of galaxies with $\log M_*/M_\odot < 9.8$ to lie above $\Sigma_* \approx 10^{8.3}\,M_\odot$ kpc^{-2}—the 1-σ lower bound to the high-mass sample's surface densities. This fraction is close to that independently obtained by extrapolating $dF_{\rm red}/dt$ above. Combined with the fact that these systems will, by definition, be the smallest low-mass galaxies—and therefore also the *reddest* (Figure 9)—this finding strengthens the conclusion that such systems were in place long ago, having formed alongside their massive counterparts. This is consistent with Toloba et al. (2015), who find low-mass galaxies with higher stellar velocity dispersions at fixed mass to have lower r_e and lie closer to the cluster core in Virgo, and therefore be older than larger-r_e systems.

Notably, the same density calculation reveals only 6% of low-mass *field* passive galaxies to have densities consistent with high-mass passive objects. If we assume, following Geha et al. (2012), that all of these dense systems are in fact stripped satellites—i.e., they do not truly arise from the same processes generating high-mass passive galaxies—this estimate can be taken as our measurement uncertainty.

As such, combined with the $dF_{\rm red}/dt$ results, we can state the following: regarding the formation of most high-mass and 10%–30% of $\log M_*/M_\odot < 9.8$ passive cluster galaxies, clusters mark regions of space where evolution was *accelerated* due to a population's residence in a common overdensity. That is, perhaps *all* sufficiently dense cluster galaxies—regardless of stellar mass—are consistent with having arisen through a

common, prompt, formation channel. This scenario—consistent with that of Dressler (1980), Abramson et al. (2016), and Kelson et al. (2016)—is fundamentally different from the environmental quenching of infalling field systems that accounts for the rest of the (mainly low-mass) cluster passive galaxy population at $z \sim 0.5$, and presumably today, suggesting a dual (or bimodal) formation scenario for passive cluster galaxies (see also Poggianti et al. 2001, 2006).

A consequence of any "accelerated" growth is that passive cluster objects would lock-in the smaller sizes of *all* star-forming galaxies *everywhere* at early epochs, appearing naturally at the bottom of the size distribution for their "final mass" and exhibiting globally higher Sérsic indices, precisely as seen in Figures 7 and 9. This effect would also naturally lead to the color–size anticorrelation revealed by our holistic fit ($\beta_{\rm UV} = -0.29 \pm 0.01$; Figure 11), which is therefore actually a reflection of the well-known redshift–size anticorrelation (e.g., Newman et al. 2012, 2014; van der Wel et al. 2014; Morishita et al. 2015) that our analysis also reveals ($\beta_z = -1.06 \pm 0.14$). The evidence of the accelerated grown in dense environment is also observed in a higher redshift cluster (e.g., Papovich et al. 2012; Bassett et al. 2013, though limited to massive galaxies).

In sum, our results point to an identifiable "native" population of galaxies at all masses that matured rapidly at early times *because* it was situated in a region of space that was also collapsing quickly. This is the mechanism that reaches to large distances, causing the population differences between clusters and the field to extend to many virial radii (Lewis et al. 2002; Treu et al. 2003; Dressler et al. 2013). To this is added a frosting of new galaxies at late times driven by something akin to ram pressure stripping or starvation (certainly something gentle), which is especially active at small clusto-centric radii and later epochs.

5.3. Better Tests than Scaling Relations

The HFF provides something close to the best possible imaging data acquirable for objects in the distant universe. As such, it is unclear what more-detailed studies of the size–mass relation will uncover in terms of offsets between mean sizes of populations as a function of environment that cannot be gleaned already.

Our approach in Section 4 points to the fundamental limitations of ever more sophisticated analysis of these kinds of galaxy-integrated, photometric metrics. Instead, our analysis suggests that, if one seeks better knowledge of the detailed physical mechanisms transforming galaxies in clusters (or outside of them), different kinds of data are required. Principally, the addition of *spectroscopic* data, and probably in a spatially resolved sense; i.e., deep and wide IFU surveys investigating the star formation and kinematic properties that may differentiate galaxies as a function of mass and environment.

For example, using light-weighted stellar ages, $\log M_*/M_\odot > 9.8$ passive galaxies observed in local clusters and the field have been seen to show a similar trend to our $\log M_*/M_\odot < 9.8$ systems, such that the largest-r_e galaxies are the youngest (e.g., Valentinuzzi et al. 2010; Poggianti et al. 2013). At $z \sim 0.5$, we see no significant color–size trend for equal-mass galaxies in this regime, but $U - V$ colors are limited as an age indicator: any passive galaxies with ages >2 Gyr would be uniformly red in this index. Hence, deep optical spectroscopy of our sample is needed to determine whether any real evolution at these masses takes place in the ~5 intervening Gyr.

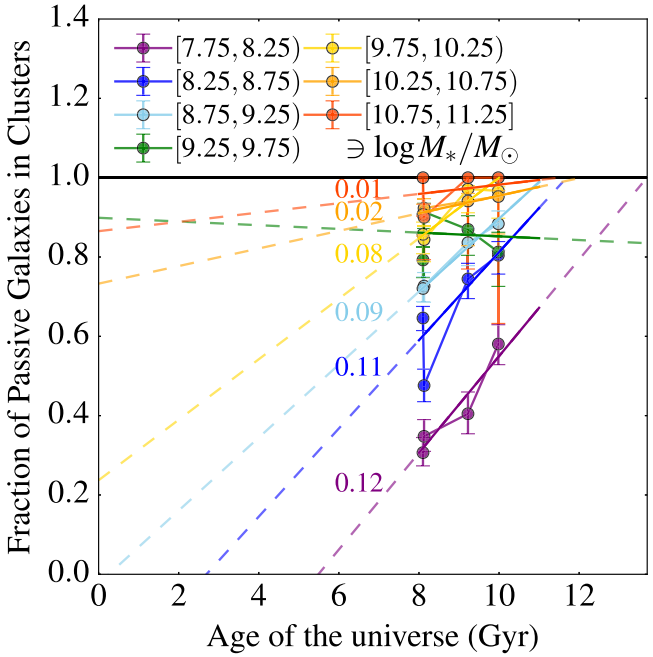

Figure 13. Extrapolation of the current quenching rate to high lookback times as a function of stellar mass. Each color corresponds to stellar mass bin listed in legend. The derived linear fit slope, $dF_{\rm red}/dt$, for each stellar mass bin is shown near the fitting line in the same color. One stellar mass bin, $9.25 < \log M_*/M_\odot < 9.75$ (green), has a negative slope, $dF_{\rm red}/dt = -0.004$, because of a weak statistics, and the value is not shown.

Also, the observed scatter in r_e could be due to radial stellar migration and not age. Induced by stellar feedback, such migration can cause r_e to fluctuate by ~2× in just ~100 Myr (e.g., El-Badry et al. 2016). We see a clear correlation between color and galaxy size, which suggests such rapid effects are not the principal source of scatter in $r_e(M_*)$ in the low-mass population, but resolved spectroscopy would constitute a much more stringent physical constraint.

The GLASS (Jones et al. 2015; Treu et al. 2015; Vulcani et al. 2015, 2016b, 2016a), GASP (Poggianti et al. in preparation), SAURON (Davies et al. 2001), ATLAS3D (Cappellari et al. 2011), 3D-*HST* (Brammer et al. 2012; Nelson et al. 2015), CALIFA (Sánchez et al. 2012), MANGA (Bundy et al. 2015), SAMI (Allen et al. 2015), amd KROSS (Magdis et al. 2016) have already started these investigations, and highly resolved analyses (mainly at low-z) show both signs of accelerated evolution driven by clusters (McDermid et al. 2015), and stripping (Conselice et al. 2001, 2003; Nipoti et al. 2003; Janz et al. 2016). By studying the sites of star formation (Wang et al. 2015, 2016) and kinematics (e.g., KLASS; Mason et al. 2016) through resolved gas maps at high(er)-z using the next generation of ground- and space-based instruments, we may be able to map the evolving importance of these effects at levels of detail currently available only in the local universe.

6. Summary

We derived photometric redshifts, stellar masses, and structural parameters for >3900 cluster and field galaxies at $0.2 \leqslant z \leqslant 0.7$ from the HFF and GLASS programs, complete

to $\log M_*/M_\odot = 7.8$—an unexplored regime at these redshifts. Using this homogeneous sample:

1. We studied the size–mass relations of four "canonical" populations—cluster/field, passive/star-forming galaxies—fitting each subsample with a single slope. Though the populations reside in environments of maximally different density, $\sim$ a factor of 1000, we find the relations to be identical within their measurement uncertainties (Figure 6). This holds even at the lowest masses where cluster-specific effects would be expected to have the most significant impact on galaxy structure.
2. A multivariate analysis—wherein all galaxy classifications are removed and sizes are fit as a function of stellar mass, Sérsic index, color, redshift *and* environment—is consistent with the above results, and quantitatively reveals local density to induce but a 7% $\pm$ 3% reduction in size (95% confidence) when controlling for these other factors (Figure 11). Immediate environment therefore appears to have a tiny effect on galaxy size, while stellar mass and color correlate most strongly.
3. We studied the trends in $(U - V)$ color in the low-mass passive cluster population ($\log M_*/M_\odot < 9.8$) as a function of offset from the best-fit slope of *star-forming* galaxies at the same redshift. We find that smaller-size galaxies are also redder.
4. The *largest*-size low-mass passive cluster galaxies—which are also the bluest—have sizes and Sérsic indices similar to those of contemporaneous star-forming galaxies (Figure 7, 8). This fact suggests that they are recently acquired systems that have been "quenched" by a cluster-specific process that terminates star formation in a non-violent manner/preserves the structure of star-forming galaxies. Given that our clusters all harbor dense intra-cluster gas, the most likely candidate is ram pressure stripping or starvation.
5. This explanation holds for the *smallest* low-mass passive cluster galaxies only if the progenitors of our clusters were capable of hosting a hot intra-cluster medium at $z \gtrsim 3$. If not, the consistent stellar surface densities and colors of these objects with those of their uniformly ancient, more massive ($\log M_*/M_\odot > 9.8$) peers suggest that 10%–30% of these galaxies are "native," having had their evolution accelerated—not terminated—by their presence in a large overdensity at birth.

Our conclusion is therefore not that environment has no impact on galaxy evolution, but rather that it *encodes* the fact that most high-mass and $\sim$18% of low-mass passive galaxies found in dense regions at late times had common (accelerated) evolutionary trajectories, with late-time effects playing some role, but only dominant at low masses.

The authors thank an anonymous referee for carefully reading our manuscript and a number of insightful suggestions. The authors thank Anton Kokoemoer and HFF team for producing and making publicly available their data. We are very grateful to the staff of the Space Telescope for their assistance in planning, scheduling and executing the observations. Support for GLASS (HST-GO-13459) was provided by NASA through a grant from the Space Telescope Science Institute, which is operated by the Association of Universities for Research in Astronomy, Inc., under NASA contract NAS 5-26555. Support for this work is provided by NASA through a Spitzer award issued by JPL/Caltech, HST-AR-13235 and HST-GO-13177. This study made use of a number of programs provided by the *Astropy* software community (Muna et al. 2016). T.M. acknowledges support from the Japan Society for the Promotion of Science (JSPS) through JSPS research fellowships for Young Scientists. B.V. acknowledges the support from an Australian Research Council Discovery Early Career Researcher Award (PD0028506). A.H. acknowledges support by NASA Headquarters under the NASA Earth and Space Science Fellowship Program—Grant ASTRO14F-0007.

Appendix A
ICL Subtraction

Each CLS pointing contains a substantial amount of diffuse intra-cluster light (ICL). Although $z_{\rm phot}$ and stellar mass estimates are not significantly affected by its presence (Figure 14; scatters are <0.1 dex), it is brightest in F160W, which we use for our primary structural measurements. Hence, to minimize possible biases in galaxy parameters, we opt to work with ICL-subtracted images.

Here, we outline the method we developed to consistently subtract a non-parametric ICL component from all CLS images. The procedure makes use of a first round of GALFIT fitting results (Section 3) as follows:

1. Single Sérsic fitting: we first fit each galaxy in a 300×300 pixel postage stamp (>80 kpc in our redshift range). We assume a single Sérsic profile and constant sky background (see Section 3).
2. Reconstruction: using the best fit sky backgrounds, we reconstruct an ICL-only (i.e., background-only) image. The value for each pixel in the map is the GALFIT background estimate at that location. For pixels with multiple postage stamps overlap, the median is calculated by weighting GALFIT's returned χ^2/ν.

We perform this procedure consistently across all HFF bands (Section 2.1).

We stress that, in contrast to previous studies (Castellano et al. 2016; Livermore et al. 2016), we assume nothing about the ICL profile, but only that single Sérsic profiles well describe *non*-ICL components (i.e., individual galaxies).

Some background fluctuations arise from non-ICL components, e.g., zodiacal light in F105W (Brammer et al. 2014), but these are small compared to the ICL. Further details of the method are discussed in Morishita et al. (2016).

Appendix B
Photo-z Priors

When deriving photometric redshifts with EAZY, we multiply the output likelihood distributions by a prior to obtain a best posterior solution. As mentioned in Section 2.3.1, we apply one of two different priors for a given galaxy depending on which pointing it is drawn from.

For PR1 sources—mainly field galaxies—we adopt the baseline EAZY prior derived from TAO lightcones for the F160W-band. The dashed lines in Figure 15, left, show these priors, which basically impose the reasonable assumption that apparently brighter objects are more likely to lie at lower redshifts.

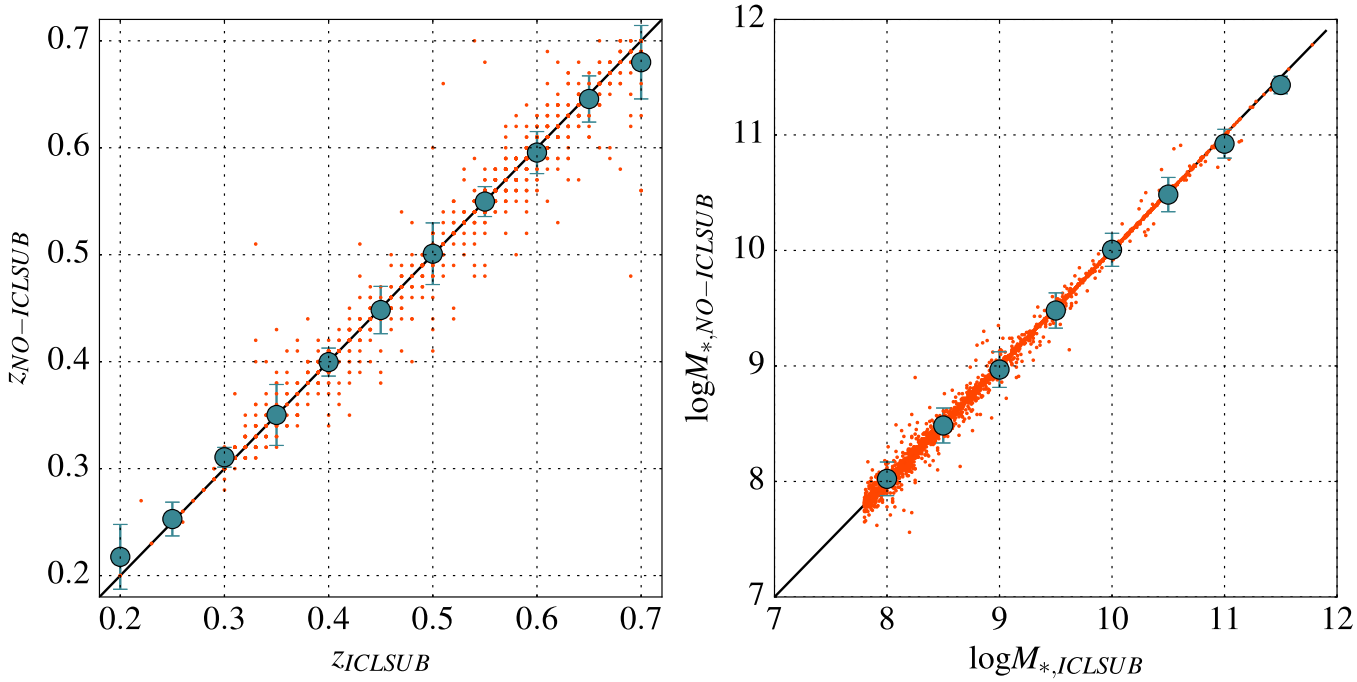

Figure 14. Comparisons of photometric redshifts (left) and stellar masses (right) estimated before and after ICL-subtraction. Median and normalized median absolute deviation for each redshift and stellar mass bin are shown (blue points with error bars).

For CLS sources, we modify the above to include the fact that we *know* a cluster lies along the line of sight. Because a large fraction of galaxies in CLS pointings will therefore be cluster members, we add to the the PR1 prior a Gaussian centered at the known cluster redshift of width $\sim$2000 km s^{-1}, roughly double the cluster velocity dispersion. We weight the contribution of the field and Gaussian prior components by f, the fraction of objets PR1 over those in CLS in bins of apparent magnitude (see main text Equation (1)). For more details about using priors in EAZY, see Brammer et al. (2008, 2011).

The assignment of weights is shown in the right panel of Figure 15, and the full CLS prior (for Abell 2744; $z_{\rm cls} = 0.308$) is shown by the solid lines at left. As expected, an excess of galaxies in CLS emerges over $18 \lesssim m_{\rm F160W} \lesssim 24$ ($f < 1$), where cluster members dominate the source counts.

The factor f exceeds unity at the brightest magnitudes, where stars (rather than cluster members) begin to dominate and sample statistics are weak. We cap the weights, however, at the physically motivated ceiling of $f = 1$, denoting that 100% of sources at that magnitude are *not* cluster members.

The weighting factor f is well described by the following analytic form,

$$f(x) = \min[1,\ 238.8 - 42.8x + 2.9x^2 - 0.08x^3 + 0.0009x^4], \quad (8)$$

where $x = m_{\rm F160W}$. This relation is shown by the red line in Figure 15, right.

Finally, Figure 16 shows the same $z_{\rm phot}$–$z_{\rm spec}$ comparison as in Figure 1, but without CLS prior. Here, we see the photometric redshifts are more widely scattered at the known cluster redshifts, with $\delta z = 0.0181$ compared to $\delta z = 0.0073$ obtained using the prior (Section 2.3.1).

Appendix C
Details On Galaxy Structure Fitting

Galaxy structural parameters are derived with GALFIT (Peng et al. 2010) as in Morishita et al. (2014). Although we only discuss F160W-band half-light radii (r_e) and Sérsic indices (n) in this study, we perform independent fits in all HFF filter bands so as to be able to characterize (and subtract) the ICL (see Appendix A).

In the CLS pointing, we re-estimate the structural parameters after subtracting the ICL, while in PR1 we adopt the first fitting results. This reduces the contamination by ICL, which varies from source to source. Our fitting procedure is as follows.

1. A PSF is empirically constructed using on-image stars with nearby sources masked and local backgrounds correctly subtracted. The TinyTim model is not used because it deviates noticeably from the observed PSF and would lead to underestimated effective radii (Morishita et al. 2014).
2. A postage stamp of 200 × 200 pixel for PR1 and 300 × 300 pixel for CLS sources is extracted, centered on the Galaxy to be fit. This stamp size difference comes from the fact that cluster centers are crowded, making identification and simultaneous fitting of neighboring objects more critical.
3. An error map is prepared by cutting the same-size stamp from the image rms map. This is fed to GALFIT as the "sigma image."
4. Other neighboring objects within the same stamp are identified and slated for simultaneous fitting if:
   (i) they are brighter than 18 mag (BCGs), or
   (ii) they are 1 mag brighter than the target galaxy and reside within 100 pixel ($\sim$40 kpc at $z \sim 0.5$).

Other neighbors are masked.

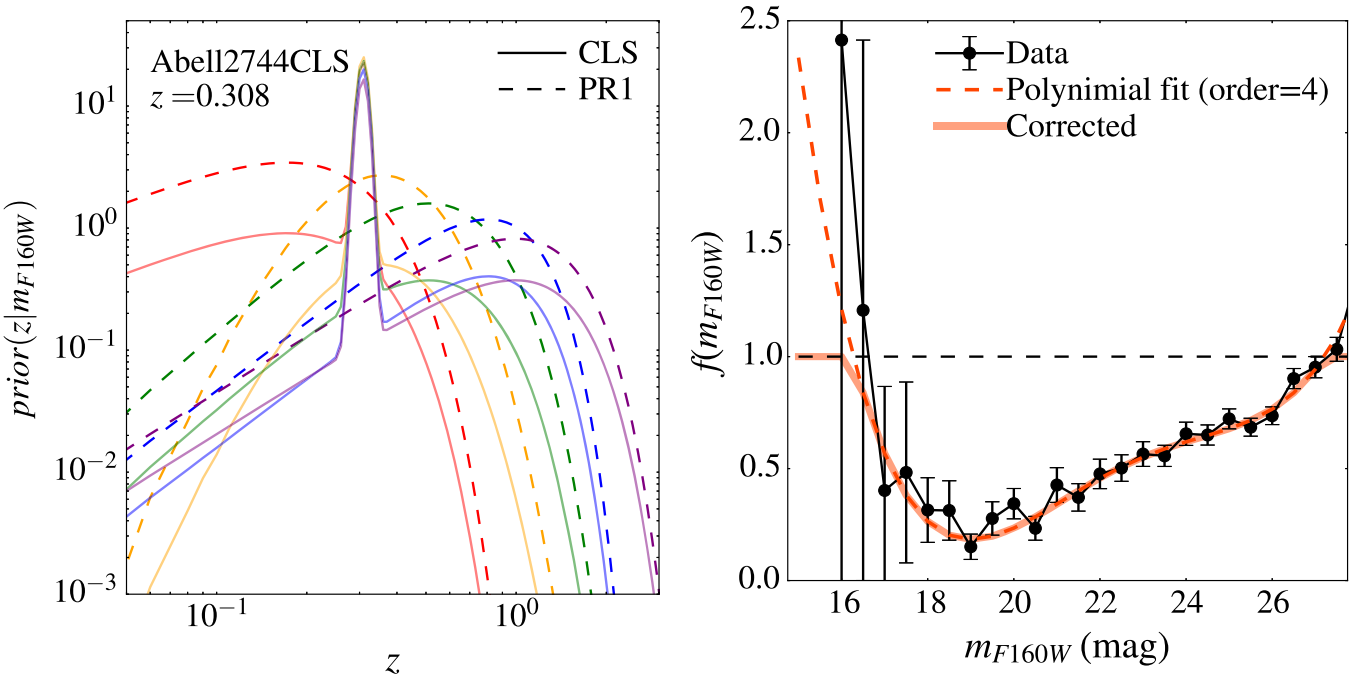

Figure 15. Left: photometric redshift priors for PR1 (dashed lines) and CLS (solid lines) provided to EAZY. The CLS prior is for Abell 2744, where we see a strong peak at cluster redshift, $z = 0.308$. Red to purple lines correspond to $m_{\rm F160W} = 19$ mag to 23 mag. Middle: fraction of the galaxies in PR1 over those in CLS in each magnitude bin (black points). The error is calculated by assuming binomial distribution. The best fit with a four-ordered polynomial fit is shown with dashed red line. The fit is then corrected not to exceed unity (horizontal dashed black line) and shown with solid red line.

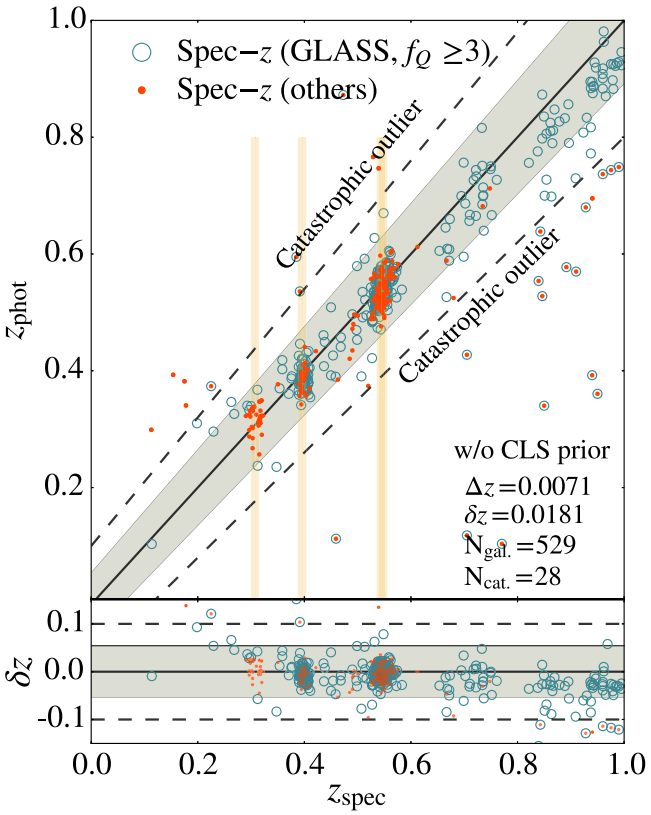

Figure 16. Same as Figure 1 in the main text, but the phot-z is derived without the cluster prior. We see the photometric redshift is more widely scattered at the cluster redshifts, as is also represented in the redshift scatter, $\delta z = 0.0181$. We also note that scatters at other redshifts (e.g., $z_{\rm spec} \sim 0.2$ and $z_{\rm spec} > 0.7$) still remain in this plot, indicating these scatters are not caused by the cluster prior.

5. A mask image is constructed based on the SExtractor segmentation map. This is convolved with a Gaussian (kernel size is 1.5 pixel), to cover faint outer envelopes. The pre- and post-convolution masks are then added to make the final mask sent to GALFIT. (Some small pixels fall under the original masking threshold after convolution and so must be replaced).
6. GALFIT is then run using the above mask and error images to fit a single Sérsic profile to the target galaxy. SExtractor outputs are taken as the initial guesses for the relevant structural parameters (centroid, position angle, ellipticity, half-light radius), with Sérsic indices initially set to 2.5 (fits are robust to this assumption). We constrain the GALFIT outputs to $|\delta m| < 1$ mag, $|\delta x| < 3$ pixel, $|\delta y| < 3$ pixel, where δ is defined with respect to the initial SExtractor values, $0.01 < 150$ pixel, and $0.1 < n < 8$. Fitting is deemed " successful" when the GALFIT outputs are within (but not at) the above limits, those failed are excluded from analysis (Appendix D).
7. We also fit the background value as a free parameter, with initial value set to 0. This component is assumed to be spatially constant across the stamp. As noted before, we use the best fit sky value of each postage stamp for reconstructing the ICL map.

This procedure is reiterated after subtracting the ICL in CLS pointings.

Notably, though the *HST* pipeline automatically subtracts a sky background, the final PR1 science images do show non-zero sky levels. These are likely due to time-varying zodiacal light. Hence, a background component is needed for both CLS and PR1 pointings, though it is not further analyzed in the latter.

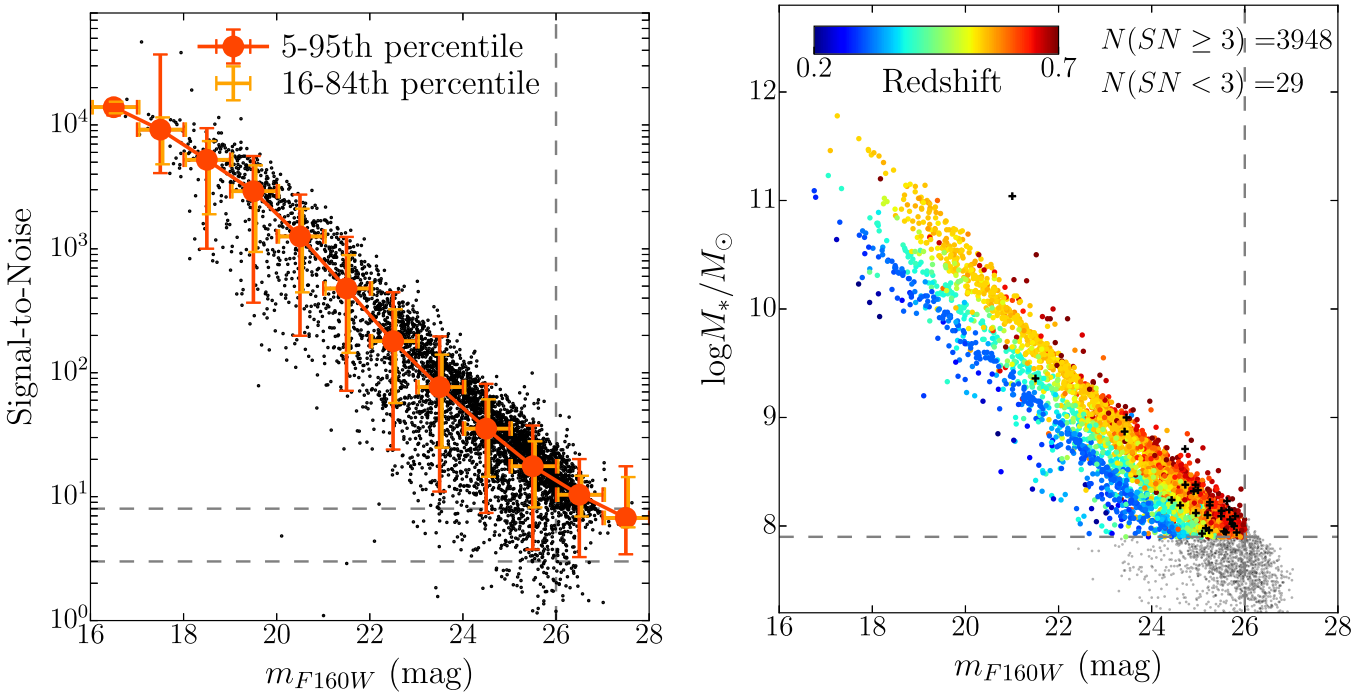

Figure 17. Left: F160W-band signal-to-noise (S/N) ration vs. apparent F160W-band magnitude. Median with 5–95th (16–84th) percentile error for each magnitude bin is shown in red (orange) crosses. In the faintest magnitude bin ($25 < m_{\rm F160W} < 26$), more than 95% of sample are S/N > 3, and >84% are S/N > 8, where reliable structural parameter can be obtained. Right: apparent magnitude (F160W)-stellar mass plots for our sample. Selected samples ($N = 3948$) above the magnitude ($m_{\rm F160W} < 26.0$) and stellar mass limit ($\log M_*/M_\odot > 7.8$) are color-coded as a function of redshift. Excluded samples with $S/N_{\rm F160W} < 3$ are shown with black crosses ($N = 29$).

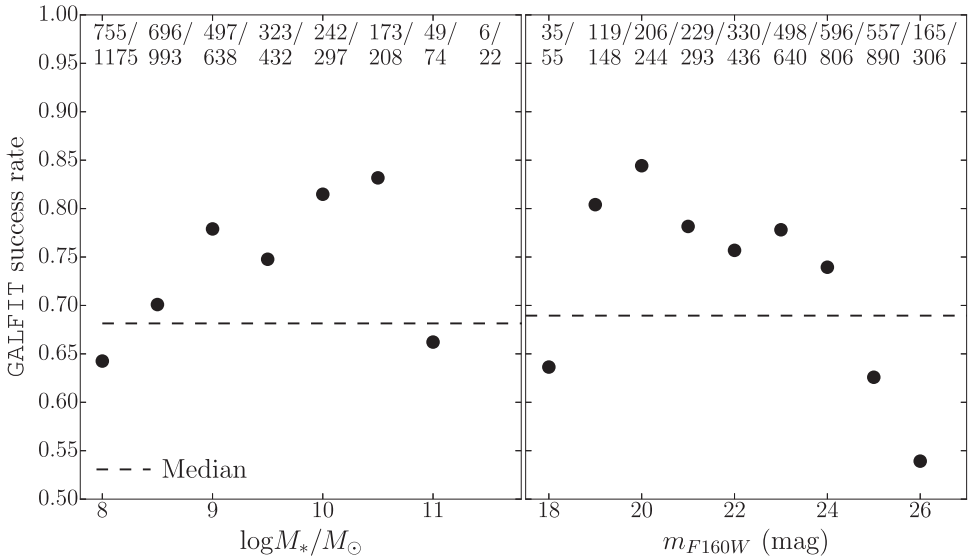

Figure 18. GALFIT success rate (black points) as a function of stellar mass (left) and F160W-band magnitude (right). Median success rate for whole sample, ≈0.77, is shown with dashed lines. The numbers shown at the top are sample numbers of success and input galaxies at each stellar mass/magnitude bins.

Appendix D
Detection Completeness, Stellar Mass Limit, and Galfit Completeness

Principally, our sample is magnitude-limited to $m_{\rm F160W} < 26.0$, reflecting the S/N required to obtain reliable structural parameters. Figure 17, left, shows the distribution of our sample in apparent F160W-band magnitude-S/N space. More than 95% of sample are S/N > 3, and >84% are S/N > 8, where others have confirmed that reliable structural parameter can be obtained (e.g., Schmidt et al. 2014b). Cutting our sample at S/N > 8 would increase the success rate in GALFIT (see below), but none of our final results would be significantly affected.

The above flux limit translates into a stellar mass limit based on the FAST results (Section 2.5). Figure 17, right, shows the relation between $m_{\rm F160W}$, redshift, and inferred stellar mass for our sample. At the highest redshifts probed, $m_{\rm F160W} = 26.0 \mapsto \log M_*/M_\odot = 7.8$, hence we adopt this as our final mass completeness limit.

As shown in Figure 18, at these stellar mass (left) and magnitude (right), ∼55% of all sources return successful fits. As the *detection* limit is much deeper ($m_{\rm F160W} \sim 28.7$ in both HFF and XDF; Kawamata et al. 2016; Lotz et al. 2016), this ensures that all galaxies that can be fit are indeed present in the data, bias in the population of successfully fit sources is minimal. At these masses, the principal cause of a GALFIT mis-measurement is the presence of a (bright) near-neighbor, a spike in ICL residuals, point sources, or a merger/other violent interaction, as well as faint/noisy objects with $3 < S/N < 8$. These are visually identified and excluded from the analysis, though their distribution is shown by the open squares in Figure 5, and are flagged in the published catalog. The fitting success rate also drops at the highest masses (Figure 17, right). This is clearly not due to S/N limits, but rather from the fact that such galaxies are large enough that their intrinsic morphological complexity—bars, spiral arms, etc.—starts to matter in the fitting process. As the total number of these objects is small however, this fact does not quantitatively affect any of our conclusions.

The number of input galaxies are 3948, within our magnitude ($m_{\rm F160W} < 26$ mag) and stellar mass/redshift criteria. Out of the input galaxies, GALFIT converges for 3666. "Successful" fits are those whose derived parameters fall within the following limits.

1. Centroids and magnitudes to within 3 pixels (in x and y) of the SExtractor input values, respectively.
2. $0.1 < n < 8$, and $q > 0.2$.

After excluding fits that do not meet the above criteria, our final catalog contains 2768 galaxies with robust structural parameters. This corresponds to a success rate of ∼67%, rising from ∼64% at $\log M_*/M_\odot \sim 8.0$ to >80% at $\log M_*/M_\odot \sim 10.0$ (Figure 18, left), or ∼53% at $m_{\rm F160W} \sim 26$ to >80% at $m_{\rm F160W} \sim 20$ (Figure 18, right).

Appendix E
MCMC

All best-fit results—for the canonical size-mass relations (3-parameter; Section 3) and the holistic characterization (7-parameter; Section 4)—are derived using the EMCEE MCMC code by Foreman-Mackey et al. (2013). This approach enables us to appropriately account for any correlations among the fitting parameters, and also disentangle the intrinsic scatter in the relations from all observational errors.

As an example of our procedure, here we illustrate how to derive our canonical size–mass relation results.

First, set $y = \log r_e/{\rm kpc}$ and $x = \log M_*/M_\odot$. Observed quantities are then represented by

$$x_i = \bar{x}_i + \epsilon_{x,i},\ y_i = \bar{y}_i + \epsilon_{y,i}, \tag{9}$$

where $\bar{x}_i$ and $\bar{y}_i$ are intrinsic values (which we never know), and $\epsilon_{x,i}$, $\epsilon_{y,i}$ are the (modeled) measurement errors in x and y of ith galaxy. We assume that errors are Gaussian, such that x_i and y_i can be represented by normal distributions, N, with variances $\sigma^2_{x,i}$, $\sigma^2_{y,i}$. Hence

$$x_i = N(\bar{x}_i, \sigma^2_{x_i}),\ y_i = N(\bar{y}_i, \sigma^2_{y_i}). \tag{10}$$

We adopt errors from FAST as σ_x and from GALFIT as σ_y.

Now, we can perform the regression. We adopt a normal linear regression model in literature,

$$\bar{y} = \alpha + \beta(\bar{x} - M_{\rm Norm}) + \sigma, \tag{11}$$

where we set $M_{\rm Norm} = 9.0$—the median mass of our sample—as the pivot point. This location is chosen so as to minimize covariance in the slope/intercept parameter uncertainties. The parameters are $\boldsymbol{\theta} = (\alpha, \beta, \sigma^2)$, where σ is the intrinsic scatter.

We set 20 (50) random walkers for 3 (7)-parameter fitting, and perform 10,000 MCMC iterations. Derived parameter estimates and uncertainties are shown in Figures 6 and 12, respectively. It is noted that, though we do not fully sample the covariance of parameters in the full fit, we believe this has little impact on the final parameter values as no strong correlation between any of parameter pairs emerges in in Figure 12.

References

Abramson, A., Kenney, J. D. P., Crowl, H. H., et al. 2011, AJ, 141, 164
Abramson, L. E., Gladders, M. D., Dressler, A., et al. 2016, ApJ, 832, 7
Abramson, L. E., & Morishita, T. 2016, ApJL, submitted (arXiv:1608.07577)
Allen, J. T., Croom, S. M., Konstantopoulos, I. S., et al. 2015, MNRAS, 446, 1567
Allen, R. J., Kacprzak, G. G., Glazebrook, K., et al. 2016, ApJ, in press (arXiv:1605.05314)
Annunziatella, M., Mercurio, A., Biviano, A., et al. 2016, A&A, 585, A160
Auger, M. W., Treu, T., Bolton, A. S., et al. 2010, ApJ, 724, 511
Balestra, I., Mercurio, A., Sartoris, B., et al. 2016, ApJS, 224, 33
Bassett, R., Papovich, C., Lotz, J. M., et al. 2013, ApJ, 770, 58
Bell, E. F., McIntosh, D. H., Katz, N., & Weinberg, M. D. 2003, ApJS, 149, 289
Bernyk, M., Croton, D. J., Tonini, C., et al. 2016, ApJS, 223, 9
Bertin, E., & Arnouts, S. 1996, A&AS, 117, 393
Bialas, D., Lisker, T., Olczak, C., Spurzem, R., & Kotulla, R. 2015, A&A, 576, A103
Binggeli, B., Sandage, A., & Tarenghi, M. 1984, AJ, 89, 64
Bolton, A. S., Burles, S., Treu, T., Koopmans, L. V. E., & Moustakas, L. A. 2007, ApJL, 665, L105
Brammer, G., Pirzkal, N., McCullough, P., & MacKenty, J. 2014, Time-varying Excess Earth-glow Backgrounds in the WFC3/IR Channel, Tech. Rep., WFC3 2014-03
Brammer, G. B., van Dokkum, P. G., & Coppi, P. 2008, ApJ, 686, 1503
Brammer, G. B., van Dokkum, P. G., Franx, M., et al. 2012, ApJS, 200, 13
Brammer, G. B., Whitaker, K. E., van Dokkum, P. G., et al. 2011, ApJ, 739, 24
Bruzual, G., & Charlot, S. 2003, MNRAS, 344, 1000
Bundy, K., Bershady, M. A., Law, D. R., et al. 2015, ApJ, 798, 7
Butcher, H., & Oemler, A., Jr. 1978, ApJ, 219, 18
Calzetti, D., Armus, L., Bohlin, R. C., et al. 2000, ApJ, 533, 682
Cappellari, M., Emsellem, E., Krajnović, D., et al. 2011, MNRAS, 413, 813
Castellano, M., Amorín, R., Merlin, E., et al. 2016, A&A, 590, A31
Cayatte, V., van Gorkom, J. H., Balkowski, C., & Kotanyi, C. 1990, AJ, 100, 604
Chabrier, G. 2003, PASP, 115, 763
Conselice, C. J., Gallagher, J. S., III, & Wyse, R. F. G. 2001, ApJ, 559, 791
Conselice, C. J., Gallagher, J. S., III, & Wyse, R. F. G. 2003, AJ, 125, 66
Damjanov, I., Abraham, R. G., Glazebrook, K., et al. 2011, ApJL, 739, L44
Davies, R. L., Kuntschner, H., Emsellem, E., et al. 2001, ApJL, 548, L33
Djorgovski, S., & Davis, M. 1987, ApJ, 313, 59
Dressler, A. 1980, ApJ, 236, 351
Dressler, A., & Gunn, J. E. 1983, ApJ, 270, 7
Dressler, A., Kelson, D. D., Abramson, L. E., et al. 2016, ApJ, 833, 251
Dressler, A., Lynden-Bell, D., Burstein, D., et al. 1987, ApJ, 313, 42
Dressler, A., Oemler, A., Jr., Poggianti, B. M., et al. 2013, ApJ, 770, 62
Ebeling, H., Stephenson, L. N., & Edge, A. C. 2014, ApJL, 781, L40
El-Badry, K., Wetzel, A., Geha, M., et al. 2016, ApJ, 820, 131
Evrard, A. E., MacFarland, T. J., Couchman, H. M. P., et al. 2002, ApJ, 573, 7
Ferrarese, L., Côté, P., Jordán, A., et al. 2006, ApJS, 164, 334
Foreman-Mackey, D., Hogg, D. W., Lang, D., & Goodman, J. 2013, PASP, 125, 306
Franx, M., van Dokkum, P. G., Schreiber, N. M. F., et al. 2008, ApJ, 688, 770
Fukugita, M., Ichikawa, T., Gunn, J. E., et al. 1996, AJ, 111, 1748
Geha, M., Blanton, M. R., Yan, R., & Tinker, J. L. 2012, ApJ, 757, 85

Grützbauch, R., Chuter, R. W., Conselice, C. J., et al. 2011, MNRAS, 412, 2361
Guglielmo, V., Poggianti, B. M., Moretti, A., et al. 2015, MNRAS, 450, 2749
Hopkins, P. F., Kereš, D., Oñorbe, J., et al. 2014, MNRAS, 445, 581
Hubble, E., & Humason, M. L. 1931, ApJ, 74, 43
Hubble, E. P. 1926, ApJ, 64, 321
Huertas-Company, M., Shankar, F., Mei, S., et al. 2013, ApJ, 779, 29
Ilbert, O., Capak, P., Salvato, M., et al. 2009, ApJ, 690, 1236
Illingworth, G. D., Magee, D., Oesch, P. A., et al. 2013, ApJS, 209, 6
Janz, J., Laurikainen, E., Laine, J., Salo, H., & Lisker, T. 2016, MNRAS, 461, L82
Jones, T., Wang, X., Schmidt, K. B., et al. 2015, AJ, 149, 107
Kawamata, R., Oguri, M., Ishigaki, M., Shimasaku, K., & Ouchi, M. 2016, ApJ, 819, 114
Kelson, D. D., Benson, A. J., & Abramson, L. E. 2016, ApJ, submitted (arXiv:1610.06566)
Kirby, E. N., Cohen, J. G., Guhathakurta, P., et al. 2013, ApJ, 779, 102
Koester, B. P., McKay, T. A., Annis, J., et al. 2007, ApJ, 660, 221
Koyama, Y., Smail, I., Kurk, J., et al. 2013, MNRAS, 434, 423
Kriek, M., van Dokkum, P. G., Labbé, I., et al. 2009, ApJ, 700, 221
Kron, R. G. 1980, ApJS, 43, 305
Lackner, C. N., & Gunn, J. E. 2013, MNRAS, 428, 2141
Lang, P., Wuyts, S., Somerville, R. S., et al. 2014, ApJ, 788, 11
Lewis, I., Balogh, M., De Propris, R., et al. 2002, MNRAS, 334, 673
Lilly, S. J., & Carollo, C. M. 2016, ApJ, 833, 1
Lin, L., Jian, H.-Y., Foucaud, S., et al. 2014, ApJ, 782, 33
Lisker, T., Janz, J., Hensler, G., et al. 2009, ApJL, 706, L124
Livermore, R. C., Finkelstein, S. L., & Lotz, J. M. 2016, ApJ, submitted (arXiv:1604.06799)
Lotz, J. M., Koekemoer, A., Coe, D., et al. 2016, ApJ, in press (arXiv:1605.06567)
Magdis, G. E., Bureau, M., Stott, J. P., et al. 2016, MNRAS, 456, 4533
Maltby, D. T., Aragón-Salamanca, A., Gray, M. E., et al. 2010, MNRAS, 402, 282
Mantz, A., Allen, S. W., Ebeling, H., Rapetti, D., & Drlica-Wagner, A. 2010, MNRAS, 406, 1773
Martig, M., Bournaud, F., Teyssier, R., & Dekel, A. 2009, ApJ, 707, 250
Mason, C. A., Treu, T., Fontana, A., et al. 2016, ApJ, submitted (arXiv:1610.03075)
McDermid, R. M., Alatalo, K., Blitz, L., et al. 2015, MNRAS, 448, 3484
McPartland, C., Ebeling, H., Roediger, E., & Blumenthal, K. 2016, MNRAS, 455, 2994
Misgeld, I., & Hilker, M. 2011, MNRAS, 414, 3699
Momcheva, I. G., Brammer, G. B., van Dokkum, P. G., et al. 2016, ApJS, 225, 27
Moore, B., Katz, N., Lake, G., Dressler, A., & Oemler, A. 1996, Natur, 379, 613
Morishita, T., Abramson, L. E., Treu, T., et al. 2016, ApJL, submitted (arXiv:1610.08503)
Morishita, T., Ichikawa, T., & Kajisawa, M. 2014, ApJ, 785, 18
Morishita, T., Ichikawa, T., Noguchi, M., et al. 2015, ApJ, 805, 34
Muna, D., Alexander, M., Allen, A., et al. 2016, arXiv:1610.03159
Muzzin, A., Marchesini, D., Stefanon, M., et al. 2013, ApJ, 777, 18
Nelson, E. J., van Dokkum, P. G., Förster Schreiber, N. M., et al. 2016, ApJ, 828, 27
Newman, A. B., Ellis, R. S., Andreon, S., et al. 2014, ApJ, 788, 51
Newman, A. B., Ellis, R. S., Bundy, K., & Treu, T. 2012, ApJ, 746, 162
Nipoti, C., Stiavelli, M., Ciotti, L., Treu, T., & Rosati, P. 2003, MNRAS, 344, 748
Nipoti, C., Treu, T., Leauthaud, A., et al. 2012, MNRAS, 422, 1714
Oke, J. B., & Gunn, J. E. 1983, ApJ, 266, 713
Omand, C. M. B., Balogh, M. L., & Poggianti, B. M. 2014, MNRAS, 440, 843
Owers, M. S., Randall, S. W., Nulsen, P. E. J., et al. 2011, ApJ, 728, 27
Paccagnella, A., Vulcani, B., Poggianti, B. M., et al. 2016, ApJL, 816, L25
Papovich, C., Bassett, R., Lotz, J. M., et al. 2012, ApJ, 750, 93
Patel, S. G., van Dokkum, P. G., Franx, M., et al. 2013, ApJ, 766, 15
Peng, C. Y., Ho, L. C., Impey, C. D., & Rix, H.-W. 2002, AJ, 124, 266
Peng, Y.-j., Lilly, S. J., Kovač, K., et al. 2010, ApJ, 721, 193
Poggianti, B. M., Bridges, T. J., Mobasher, B., et al. 2001, ApJ, 562, 689
Poggianti, B. M., Fasano, G., Omizzolo, A., et al. 2016, AJ, 151, 78
Poggianti, B. M., Moretti, A., Calvi, R., et al. 2013, ApJ, 777, 125
Poggianti, B. M., von der Linden, A., De Lucia, G., et al. 2006, ApJ, 642, 188
Roediger, J. C., Courteau, S., MacArthur, L. A., & McDonald, M. 2011, MNRAS, 416, 1996
Salim, S., Rich, R. M., Charlot, S., et al. 2007, ApJS, 173, 267
Sánchez, S. F., Kennicutt, R. C., Gil de Paz, A., et al. 2012, A&A, 538, A8
Schlegel, D. J., Finkbeiner, D. P., & Davis, M. 1998, ApJ, 500, 525
Schmidt, K. B., Treu, T., Brammer, G. B., et al. 2014a, ApJL, 782, L36
Schmidt, K. B., Treu, T., Trenti, M., et al. 2014b, ApJ, 786, 57
Sérsic, J. L. 1963, BAAA, 6, 41
Shen, S., Mo, H. J., White, S. D. M., et al. 2003, MNRAS, 343, 978
Speagle, J. S., Steinhardt, C. L., Capak, P. L., & Silverman, J. D. 2014, ApJS, 214, 15
Spergel, D. N., Verde, L., Peiris, H. V., et al. 2003, ApJS, 148, 175
Stringer, M. J., Shankar, F., Novak, G. S., et al. 2014, MNRAS, 441, 1570
Thomas, D., Maraston, C., Bender, R., & Mendes de Oliveira, C. 2005, ApJ, 621, 673
Toloba, E., Guhathakurta, P., Boselli, A., et al. 2015, ApJ, 799, 172
Toloba, E., Guhathakurta, P., Peletier, R. F., et al. 2014, ApJS, 215, 17
Trenti, M., Santos, M. R., & Stiavelli, M. 2008, ApJ, 687, 1
Treu, T., Ellis, R. S., Kneib, J.-P., et al. 2003, ApJ, 591, 53
Treu, T., Schmidt, K. B., Brammer, G. B., et al. 2015, ApJ, 812, 114
Valentinuzzi, T., Fritz, J., Poggianti, B. M., et al. 2010, ApJ, 712, 226
van den Bosch, F. C., Aquino, D., Yang, X., et al. 2008, MNRAS, 387, 79
van der Wel, A., Franx, M., van Dokkum, P. G., et al. 2014, ApJ, 788, 28
van Dokkum, P., Brammer, G., Momcheva, I., et al. 2013, arXiv:1305.2140
van Dokkum, P. G., Whitaker, K. E., Brammer, G., et al. 2010, ApJ, 709, 1018
Vollmer, B., Soida, M., Chung, A., et al. 2009, A&A, 496, 669
Vulcani, B., Bundy, K., Lackner, C., et al. 2014, ApJ, 797, 62
Vulcani, B., Poggianti, B. M., Finn, R. A., et al. 2010, ApJL, 710, L1
Vulcani, B., Treu, T., Nipoti, C., et al. 2016a, ApJ, submitted (arXiv:1610.04615)
Vulcani, B., Treu, T., Schmidt, K. B., et al. 2015, ApJ, 814, 161
Vulcani, B., Treu, T., Schmidt, K. B., et al. 2016b, ApJ, 833, 178
Wang, X., Hoag, A., Huang, K.-H., et al. 2015, ApJ, 811, 29
Wang, X., Jones, T. A., Treu, T., et al. 2016, arXiv:1610.07558
Wetzel, A. R., Tinker, J. L., Conroy, C., & van den Bosch, F. C. 2013, MNRAS, 432, 336
Whitaker, K. E., Bezanson, R., van Dokkum, P. G., et al. 2016, ApJ, submitted (arXiv:1607.03107)
Whitaker, K. E., Franx, M., Leja, J., et al. 2014, ApJ, 795, 104
Williams, R. J., Quadri, R. F., Franx, M., van Dokkum, P., & Labbé, I. 2009, ApJ, 691, 1879
Wu, P.-F., Gal, R. R., Lemaux, B. C., et al. 2014, ApJ, 792, 16
Zanella, A., Scarlata, C., Corsini, E. M., et al. 2016, ApJ, 824, 68